







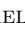















# JWST Spectroscopy of SN H0pe: Classification and Time Delays of a Triply-imaged Type Ia Supernova at $z = 1.78$

WENLEI CHEN <sup>1,2</sup> PATRICK L. KELLY <sup>2</sup> BRENDA L. FRYE <sup>3</sup> JUSTIN PIEREL <sup>4</sup> S. P. WILLNER <sup>5</sup>  
MASSIMO PASCALE <sup>6</sup> SETH H. COHEN <sup>7</sup> CHRISTOPHER J. CONSELICE <sup>8</sup> MICHAEL ENGESSEER <sup>9</sup> LUKAS J. FURTAK <sup>10</sup>  
DANIEL GILMAN <sup>11,12</sup> NORMAN A. GROGIN <sup>4</sup> SIMON HUBER <sup>13,14</sup> SAURABH W. JHA <sup>15</sup> JOEL JOHANSSON <sup>16</sup>  
ANTON M. KOEKEMOER <sup>4</sup> CONOR LARISON <sup>15</sup> ASHISH K. MEENA <sup>10</sup> MATTHEW R. SIEBERT <sup>4</sup>  
ROGIER A. WINDHORST <sup>7</sup> HAOJING YAN <sup>17</sup> AND ADI ZITRIN <sup>10</sup>

<sup>1</sup>Department of Physics, Oklahoma State University, 145 Physical Sciences Bldg, Stillwater, OK 74078, USA

<sup>2</sup>School of Physics and Astronomy, University of Minnesota, 116 Church Street SE, Minneapolis, MN 55455, USA

<sup>3</sup>Department of Astronomy/Steward Observatory, University of Arizona, 933 N. Cherry Avenue, Tucson, AZ 85721, USA

<sup>4</sup>Space Telescope Science Institute, 3700 San Martin Dr., Baltimore, MD 21218, USA

<sup>5</sup>Center for Astrophysics | Harvard & Smithsonian, 60 Garden Street, Cambridge, MA, 02138, USA

<sup>6</sup>Department of Astronomy, University of California, 501 Campbell Hall #3411, Berkeley, CA 94720, USA

<sup>7</sup>School of Earth and Space Exploration, Arizona State University, Tempe, AZ 85287-1404, USA

<sup>8</sup>Jodrell Bank Centre for Astrophysics, Alan Turing Building, University of Manchester, Oxford Road, Manchester M13 9PL, UK

<sup>9</sup>Space Telescope Science Institute, 3700 San Martin Drive, Baltimore, MD 21218, USA

<sup>10</sup>Physics Department, Ben-Gurion University of the Negev, P. O. Box 653, Be'er-Sheva, 8410501, Israel

<sup>11</sup>Department of Astronomy & Astrophysics, University of Chicago, Chicago, IL 60637, USA

<sup>12</sup>Brinson Fellow

<sup>13</sup>Max-Planck-Institut für Astrophysik, Karl-Schwarzschild-Str. 1, 85748 Garching, Germany

<sup>14</sup>Physik-Department, Technische Universität München, James-Frank-Straße 1, 85748 Garching, Germany

<sup>15</sup>Department of Physics and Astronomy, Rutgers, the State University of New Jersey, 136 Frelinghuysen Rd., Piscataway, NJ 08854, USA

<sup>16</sup>Oskar Klein Centre, Department of Physics, Stockholm University, AlbaNova, SE-10691 Stockholm, Sweden

<sup>17</sup>Department of Physics and Astronomy, University of Missouri, Columbia, MO 65211, USA

## ABSTRACT

SN H0pe is a triply imaged supernova (SN) at redshift  $z = 1.78$  discovered using the *James Webb Space Telescope* (*JWST*). In order to classify the SN spectroscopically and measure the relative time delays of its three images (designated A, B, and C), we acquired NIRSpect follow-up spectroscopy spanning 0.6 to 5  $\mu\text{m}$ . From the high signal-to-noise spectra of the two bright images B and C, we first classify the SN, whose spectra most closely match those of SN 1994D and SN 2013dy, as a Type Ia SN. We identify prominent blueshifted absorption features corresponding to Si II  $\lambda 6355$  and Ca II H  $\lambda 3970$  and K  $\lambda 3935$ . We next measure the absolute phases of the three images from our spectra, which allows us to constrain their relative time delays. The absolute phases of the three images, determined by fitting the three spectra to Hsiao07 SN templates, are  $6.5^{+2.4}_{-1.8}$  d,  $24.3^{+3.9}_{-3.9}$  d and  $50.6^{+16.1}_{-15.3}$  d for the brightest to faintest images. These correspond to relative time delays between Image A and Image B and between Image B and Image C of  $-122.3^{+43.7}_{-43.8}$  d and  $49.3^{+12.2}_{-14.7}$  d, respectively. The SALT3-NIR model yields phases and time delays consistent with these values. After unblinding, we additionally explored the effect of using Hsiao07 template spectra for simulations through eighty instead of sixty days past maximum, and found a small (11.5 and 1.0 days, respectively) yet statistically insignificant ( $\sim 0.25\sigma$  and  $\sim 0.1\sigma$ ) effect on the inferred image delays.

## 1. INTRODUCTION

Refsdal (1964) showed that, in principle, the relative time delays between the appearances of a multiply imaged supernova (SN) could be used to constrain the Hubble constant  $H_0$ . It took more than fifty years, however, to put this theory to use. The first strongly

lensed SN with multiple resolved images, dubbed “SN Refsdal” in honor of Sjur Refsdal, was discovered in 2014 (Kelly et al. 2015, 2016), and it has been used to measure  $H_0$  with competitive precision (Kelly et al. 2023). SN Refsdal occurred in a galaxy at  $z = 1.491$  (Smith et al. 2009) and was strongly lensed by the MACS J1149.5+2223 galaxy cluster. The method of measuring  $H_0$  using a SN strongly lensed by a galaxy cluster involves systematic uncertainties that are different from those of measurements that instead employ quasars that are multiply imaged by galaxy-scale lenses (e.g., Suyu et al. 2017). In particular, models of galaxy-cluster lenses have substantially less sensitivity to the mass-sheet degeneracy given strongly lensed sources at multiple redshifts, and they exhibit more modest projection effects in comparison to galaxy-scale lenses. Being lensed by a galaxy cluster, SN Refsdal also had an approximately year-long time delay, which is much longer than those from galaxy-scale lenses. This enabled more precise time-delay measurements to constrain  $H_0$ . Based on a preliminary time delay measurement of its multiple images from Kelly et al. (2016) and available model predictions, Vega-Ferrero et al. (2018) obtained  $H_0 = 64_{-11}^{+9}$  km s $^{-1}$  Mpc $^{-1}$  at 68% confidence. With a 1.5% time-delay measurement from Kelly et al. (2023), Kelly et al. (2023) performed a blind measurement of the relative time delays and magnification ratios of its multiple images with improved precision and accuracy. Based on eight independent cluster lens models, Kelly et al. (2023) inferred  $H_0 = 64.8_{-4.3}^{+4.4}$  km s $^{-1}$  Mpc $^{-1}$ . The two lens models most consistent with the observations yielded  $H_0 = 66.6_{-3.3}^{+4.1}$  km s $^{-1}$  Mpc $^{-1}$ . Recent efforts have used the 1.5% Kelly et al. (2023) time delay measurement for Refsdal in combination with additional lens models to constrain the Hubble constant for additional assumptions, and obtain measurements within  $\sim 1\text{-}\sigma$  agreement (Liu & Oguri 2024; Grillo et al. 2024).

Additional multiply imaged SNe have been found. SN Ia iPTF 16geu at  $z = 0.409$  was detected in ground-based imaging two years after SN Refsdal (Goobar et al. 2017). Two other SNe, “SN Requiem” at  $z = 1.95$  (Rodney et al. 2021) and “SN Zwicky” at  $z = 0.354$  (Goobar et al. 2022), were identified in *Hubble Space Telescope* (*HST*) data. Recently, a multiply imaged core-collapse supernova (CCSN) at  $z \approx 3$  was found in archival *HST* images taken in 2010 (Chen et al. 2022). In addition, a candidate multiply imaged SN Ia (SN 2022riv) was detected in *HST* imaging (*HST* SNAP 16729; PI: P. Kelly) and followed up by *HST* and *James Webb Space Telescope* (*JWST*) observations (*HST* 16264; PI: J. Pierel, *HST* 17253; PI: P. Kelly, and *JWST* 2767; PI: P. Kelly), making it the first strongly lensed SN ob-

served by *JWST*. However, these cases all have limitations for cosmological constraints. SN iPTF 16geu and SN Zwicky are at relatively low redshifts, and the short time delays ( $< 1$  day) between the multiple images do not allow an accurate measurement of  $H_0$  (Dhawan et al. 2020; Johansson et al. 2021). SN Requiem and the CCSN at  $z \approx 3$  lack light curves for the measurement of the relative delays, and only the trailing image of 22riv has been detected.

On 2023 March 30, a candidate SN Ia dubbed “SN H0pe” (Frye et al. 2023) appeared in the NIRC*am* images of the PLCK G165.7+67 (G165) galaxy-cluster field. SN H0pe was confirmed to be a transient when the NIRC*am* images were compared against *HST* WFC3 images taken seven years earlier. Follow-up spectroscopic observations using the Large Binocular Telescope (LBT) were also conducted, which yielded a precise redshift for the arc (Polletta et al. 2023). At  $z = 1.78$  (Polletta et al. 2023; Frye et al. 2024), SN H0pe is the highest-redshift strongly lensed SN Ia. The candidate was followed up 23 days after discovery with NIRS*pec* spectroscopy and a second epoch of NIRC*am* imaging (Figure 1), which was followed by a third NIRC*am* imaging epoch 17 days later (Frye et al. 2024). SN H0pe offers the opportunity to make a second, independent measurement of  $H_0$  using a different cluster lens.

Frye et al. (2024) described SN H0pe’s discovery and the strong lensing, photometric, and spectroscopic analysis of the G165 cluster field. This paper analyzes the spectroscopic data to determine the SN’s phase in each of its three images. Pierel et al. (2024, submitted) have analyzed photometry of SN H0pe in order to obtain an independent measurement the relative time delays among the images. An upcoming publication by Pascale et al. 2024 will present an inference of  $H_0$  based on the time-delay measurements from these spectroscopic and photometric analyses. For this study, the spectroscopic phases were measured in a blind analysis independent of the light curve and the lens modeling. In other words, we intentionally excluded imaging data and lens models from the current analysis, and the results are based only on the NIRS*pec* data and SN spectral templates.

The paper is organized as follows. Section 2 describes the *JWST* NIRS*pec* data set. Section 3 and Section 4 presents the spectral analysis of SN H0pe and its host galaxy. Section 5 describes our methods to measure the phases of the SN images. Section 6 outlines the simulation of our model and the error analysis. Section 7 presents the final constraints on the time delays and the magnifications of SN H0pe’s images. Section 8 describes the updates after we unblinded our initial results to the

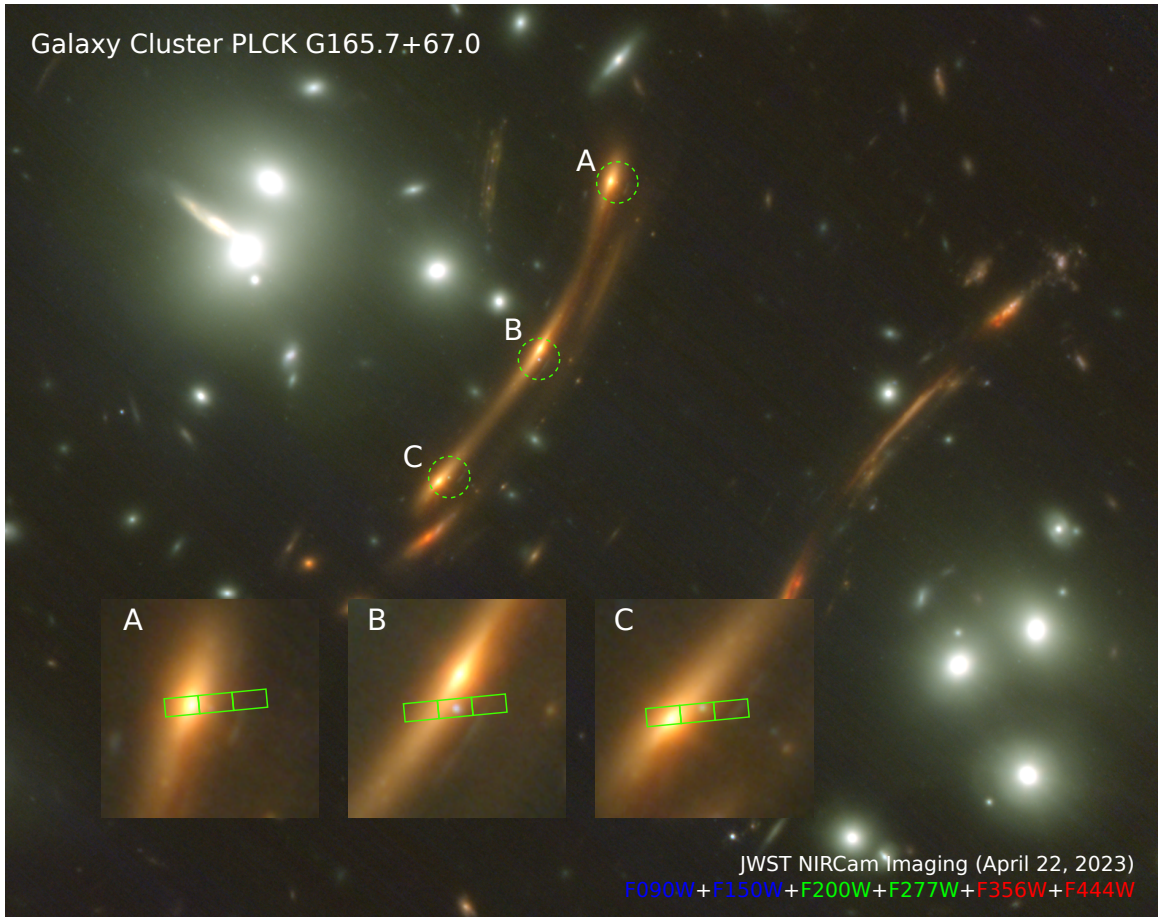


**Figure 1.** Color image of the Arc 2 region of G165. This “Epoch 2” NIRCam image was taken on 2023 April 22, the same day the spectra were acquired. Green dashed circles in the main image are centered on the three SN images, which are labeled A, B, C from north to south. The three stamp images superposed on the main image show magnified images of the SN and its host galaxy with superposed green rectangles marking the open shutters in the NIRSpec MSA. The SN is visible as a blue point source situated at the central shutter of each slitlet. North is up and east is to the left in all images, and red represents the NIRCam F356W and F444W filters, green represents F200W and F277W, and blue represents F090W and F150W. The scale of the main image is indicated by the distance from A to C, which is  $14''$ .

$H_0$ -inference team (Pascale et al. 2024). Section 9 discusses the implications and presents our conclusions.

## 2. DATA

SN H0pe was detected in *JWST* NIRCam imaging of the galaxy cluster G165 acquired on UT 2023 March 30 by the Prime Extragalactic Areas for Reionization and Lensing Science (PEARLS) program (Windhorst et al. 2023, GTO 1176; PI: R. Windhorst). Frye et al. (2024) described the data reduction and analysis and the three images of the SN and its host galaxy. The SN and its host galaxy are near the central region of the galaxy-cluster field, as shown in Figure 1. SN Images A, B, and C have R.A. and Dec. coordinates (J2000) 11:27:15.31, +42:28:41.0; 11:27:15.60, +42:28:33.8; and 11:27:15.94, +42:28:28.9, respectively (Frye et al. 2024, their Table 2).

We obtained follow-up *JWST* NIRSpec Multi-Object Spectroscopy (MOS) and NIRCam imaging on 2023 April 22 UT (“Epoch 2:” DDT 4446; PI: B. Frye). The NIRSpec observations were designed using the Micro-Shutter Assembly (MSA) to acquire spectra of the three images of SN H0pe, two of the three images of the SN host galaxy, and 42 other gravitationally lensed arcs. The SN and host galaxy spectra used three MSA slitlets (open shutters) end-to-end as shown in Figure 1. The color image was generated from the Epoch 2 NIRCam images. Each slitlet has an open area of  $0''.20$  in the dispersion direction and  $0''.46$  in the spatial direction. There is a  $0''.07$  gap between slitlets, giving a total height for three slitlets of  $1''.52$ . The NIRSpec MOS data comprised the PRISM (0.6 to  $5.3 \mu\text{m}$  wavelength coverage at spectral resolution  $R \sim 100$ ) and the G140M and G235M gratings ( $0.70$  to  $3.07 \mu\text{m}$  at  $R \sim 1000$ ).

We began processing the spectroscopic data by downloading the Stage 2 data from the Mikulski Archive for Space Telescopes (MAST). Additional processing used the *JWST* pipeline<sup>1</sup> (Bushouse et al. 2022) with context file `hwst_1087.pmap` to produce two-dimensional (2D) spectral data. The pipeline applied a slit-loss throughput correction for the SN images based on their planned positions within the MSA shutters. The spectra of the SN and its host galaxy images were extracted using the optimal extraction algorithm from Horne (1986) implemented as scripts available as part of the MOS Optimal Spectral Extraction (MOSE) notebook.<sup>2</sup> We used `webbpsf`<sup>3</sup> to generate the effective point-spread functions (PSFs) for the NIRSpec observations.

To separate the spectra of the SN and its host galaxy, we fit two kernels simultaneously to the flux in the 2D spectrum as a function of wavelength. We used a Gaussian kernel to model the flux distributions of the point source (the SN) and selected from Gaussian, Moffat (Moffat 1969), and Voigt (e.g., Whiting 1968) distribution functions to model the extended source (the host galaxy) along the spatial direction of each 2D spectrum. The kernels were chosen based on the best-fit profile functions that minimized the least-square statistic. During the extraction process, we disregarded the uncertainties related to the kernel functions. Figure 2 shows the 2D spectrum model and the extracted spectrum for the PRISM observations of Image B. Appendix A gives complete details of the extraction method and the full complement of two-dimensional spectra and source models for the SN. Frye et al. (2024) presented the full spectroscopic data set.

### 3. SPECTRUM OF THE HOST GALAXY

As shown in Figure 1, the NIRSpec slitlets placed on Images A and C intersect the host galaxy’s nucleus. Because the SN was faintest in image A, the A slitlet yields the highest signal-to-noise ratio and least-contaminated spectrum of the host galaxy. Figure 3 shows the spectrum of the host, and Table 1 lists the identifications and fluxes of the detected lines. For our analysis, we used GLEAM (Stroe & Savu 2021), a software package that uses the LMFIT Python package (Newville et al. 2021) to perform the line fitting and to calculate errors on fit parameters. The line wavelengths (excluding unresolved doublets such as [O II]) give spectroscopic redshift  $z = 1.7825 \pm 0.0008$ , which agrees with the spec-

troscopic measurement using the LBT Utility Camera in the Infrared (LUCI) (Polletta et al. 2023) and with an independent redshift measurement (Frye et al. 2024) from the same NIRSpec data. The line identifications also agree with Frye et al. (2024), who analyzed the spectroscopy of host-galaxy Images A and C (labeling them Arc 2a and 2c, respectively). They estimated the H $\alpha$  line flux with corrections for underlying stellar absorption, dust extinction, and slit loss of the whole arc. Their Table 4 gives host-galaxy specific star-formation rates (derived from the H $\alpha$  flux) and stellar masses derived from Images A and C.

### 4. SPECTRA OF SN H0PE

Figure 4 shows the extracted spectra of Images B and C. The portions within rest wavelengths 3600 Å to 10000 Å were cross matched with the SN Ia template library available in the Next Generation SuperFit (NGSF) software package (Goldwasser et al. 2022). Table 2 lists the five best-fit SN templates from NGSF. As shown in Figure 5, the SN spectra are consistent with those of a SN Ia. The spectra of Images B and C most closely match those SN 2013dy and SN 1994D at phases of 6 days and 28 days, respectively. The favored subtype is “Ia-norm,” a normal SN Ia (Blondin & Tonry 2007). Image A had the lowest signal-to-noise ratio among the three SN images, and consequently the template-matching could not yield a favored SN type or subtype. If we force the match within a set of previously observed SNe Ia, the spectrum of Image A most closely matches SN 2015N at 49 days after its peak brightness. Figure 5 shows these best-match spectra superimposed on the spectra of SN H0pe for comparison.

When the spectra were obtained, Image B was the brightest of the three SN images. As shown in Figure 4, the spectrum of Image B exhibits the Si II absorption feature near 6120 Å in the rest frame of the host galaxy. This is an identifying characteristic of SN Ia spectra (Filippenko 1997): A deep absorption trough around 6150 Å produced by blueshifted Si II  $\lambda 6355$  emission is prominent in the spectra of SNe Ia through roughly several weeks after maximum but is absent from the spectra of other types of SNe.

Typical velocities for SNe Ia near maximum light are  $v_{\text{Si II}} \approx 10\text{--}12 \times 10^3 \text{ km s}^{-1}$  and  $v_{\text{Ca II}} \approx 13\text{--}15 \times 10^3 \text{ km s}^{-1}$  (Filippenko 1997). Figure 4 shows blueshifted Si II  $\lambda 6355$  and Ca II H & K ( $\lambda 3935$ ,  $\lambda 3970$ ) absorption lines at  $6117 \pm 2 \text{ \AA}$  ( $\sim 17017 \text{ \AA}$  in the observer frame) and at  $3790 \pm 2 \text{ \AA}$  ( $\sim 10544 \text{ \AA}$  in the observer frame), respectively. These wavelengths for SN H0pe give  $v_{\text{Si II}} = -11.23 \pm 0.11 \times 10^3 \text{ km s}^{-1}$  and  $v_{\text{Ca II}} = -12.54 \pm 0.19 \times 10^3 \text{ km s}^{-1}$  relative to the host-

<sup>1</sup> <https://github.com/spacetelescope/jwst>

<sup>2</sup> [https://spacetelescope.github.io/jdat\\_notebooks/notebooks/optimal\\_extraction/Spectral\\_Extraction-static.html](https://spacetelescope.github.io/jdat_notebooks/notebooks/optimal_extraction/Spectral_Extraction-static.html)

<sup>3</sup> <https://webbpsf.readthedocs.io/en/latest/index.html>

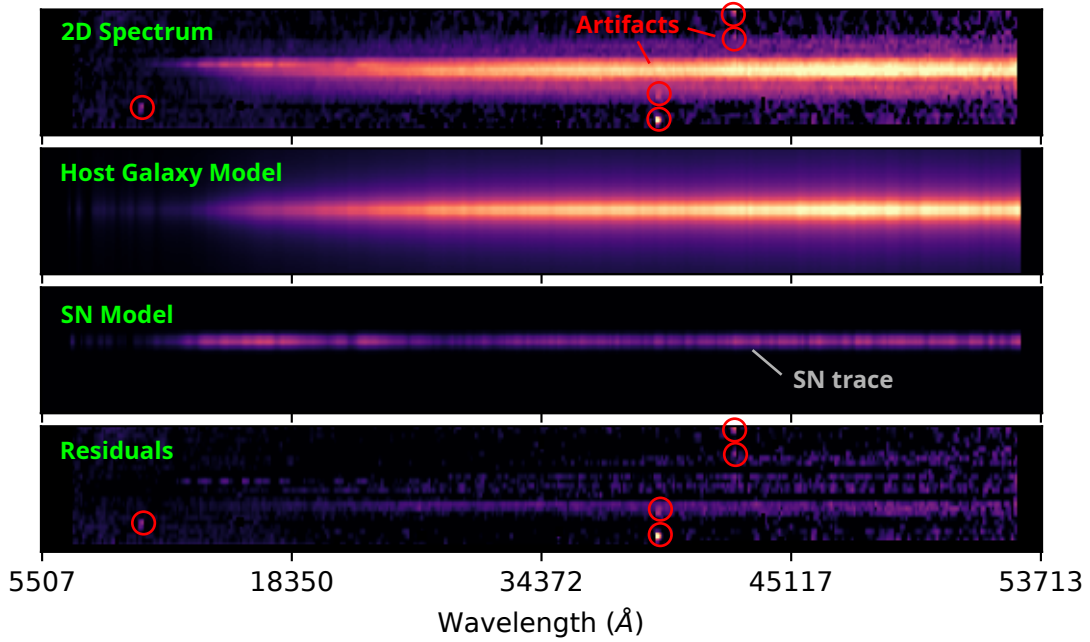


**Figure 2.** NIRSpect PRISM spectrum of the host galaxy and the SN from Slit B (Figure 1). Observed wavelengths are marked at the bottom, and the total height of each panel projects to  $1''.52$  on the sky. The top panel shows the 2D spectrum from the *JWST* pipeline. The middle two panels show the best-fit models of the host galaxy and the SN, respectively. The bottom panel shows the residuals after subtracting the galaxy and the SN models from the original spectrum. Red circles label the cosmic-ray-related artifacts (hot pixels) in the 2D spectrum.

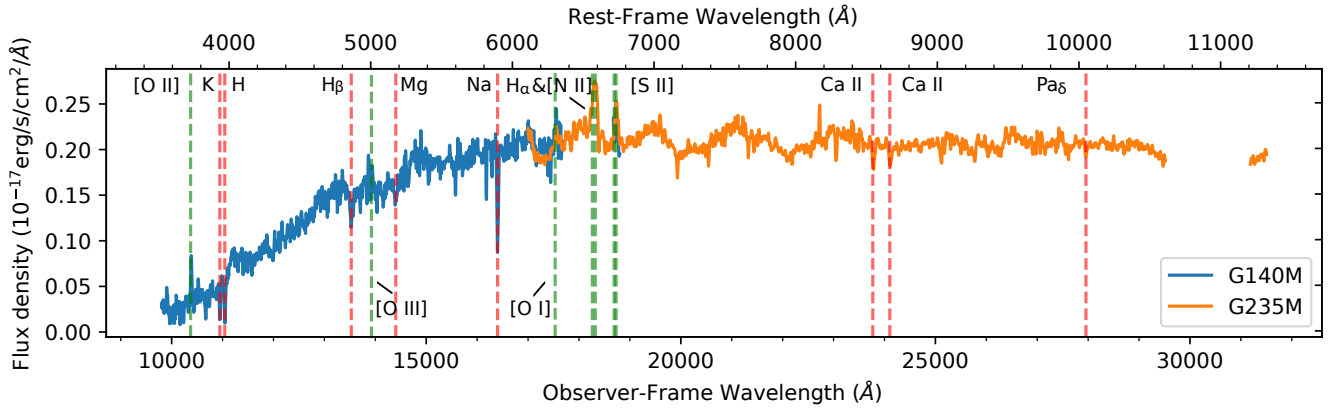


**Figure 3.** NIRSpect G140M and G235M spectra of the A image of the host-galaxy nucleus. The data are for the single  $0''.46$  slitlet containing the nucleus (Figure 1). Vertical lines mark the positions of the detected emission (green) and absorption (red) lines, as listed in Table 1. Wavelengths are marked in the observed frame (bottom) and in the  $z = 1.7825$  rest frame (top). The gap in the spectrum near observed  $3\mu\text{m}$  is from the physical gap between the two NIRSpect detector chips. The spectra and line identifications for Images A and C are also shown by [Frye et al. \(2024\)](#).

**Table 1. Emission and absorption lines of the A image of the host-galaxy nucleus.**

Spectral Line	Wavelength (rest-frame Å)	Line Flux <sup>a</sup> ( $\times 10^{-17}$ erg s <sup>-1</sup> cm <sup>-2</sup> )	EW <sup>b</sup> (Å)
[O II], [O II]	3727, 3730	$1.40 \pm 0.22$	$15.6 \pm 2.5$
Ca K	3935	$-1.13 \pm 0.26^c$	$-8.0 \pm 1.9$
Ca H	3970	$-1.86 \pm 0.40$	$-10.5 \pm 2.3$
H $\beta$	4863	$-2.09 \pm 0.32$	$-4.9 \pm 0.7$
[O III]	5008	$0.75 \pm 0.23$	$1.7 \pm 0.5$
Mg	5177	$-1.66 \pm 0.39$	$-3.6 \pm 0.8$
Na	5896	$-4.07 \pm 0.22$	$-7.3 \pm 0.4$
[O I]	6302	$1.97 \pm 0.42$	$3.5 \pm 0.7$
H $\alpha$ , [N II]	6565, 6585	$7.24 \pm 0.87$	$12.1 \pm 1.5$
[S II], [S II]	6718, 6732	$3.39 \pm 0.37$	$6.0 \pm 0.7$
Ca II	8544	$-1.41 \pm 0.17$	$-2.5 \pm 0.3$
Ca II	8665	$-1.15 \pm 0.14$	$-2.0 \pm 0.2$
Pa $\delta$	10053	$-0.65 \pm 0.10$	$-1.1 \pm 0.2$

<sup>a</sup>The flux measurements are as observed in a single slitlet, i.e., not corrected for magnification due to gravitational lensing, underlying stellar absorption, dust extinction, or slit losses. [Frye et al. \(2024\)](#) first identified the lines listed and showed spectra of host-galaxy Images A and C (labeling them Arc 2a and 2c, respectively). They also gave the H $\alpha$  line flux with corrections for underlying stellar absorption, dust extinction, and slit loss of the whole arc.

<sup>b</sup>Rest-frame equivalent widths (EWs) of emission and absorption lines.

<sup>c</sup>Negative flux and EWs indicate absorption lines, the latter opposite the usual convention.

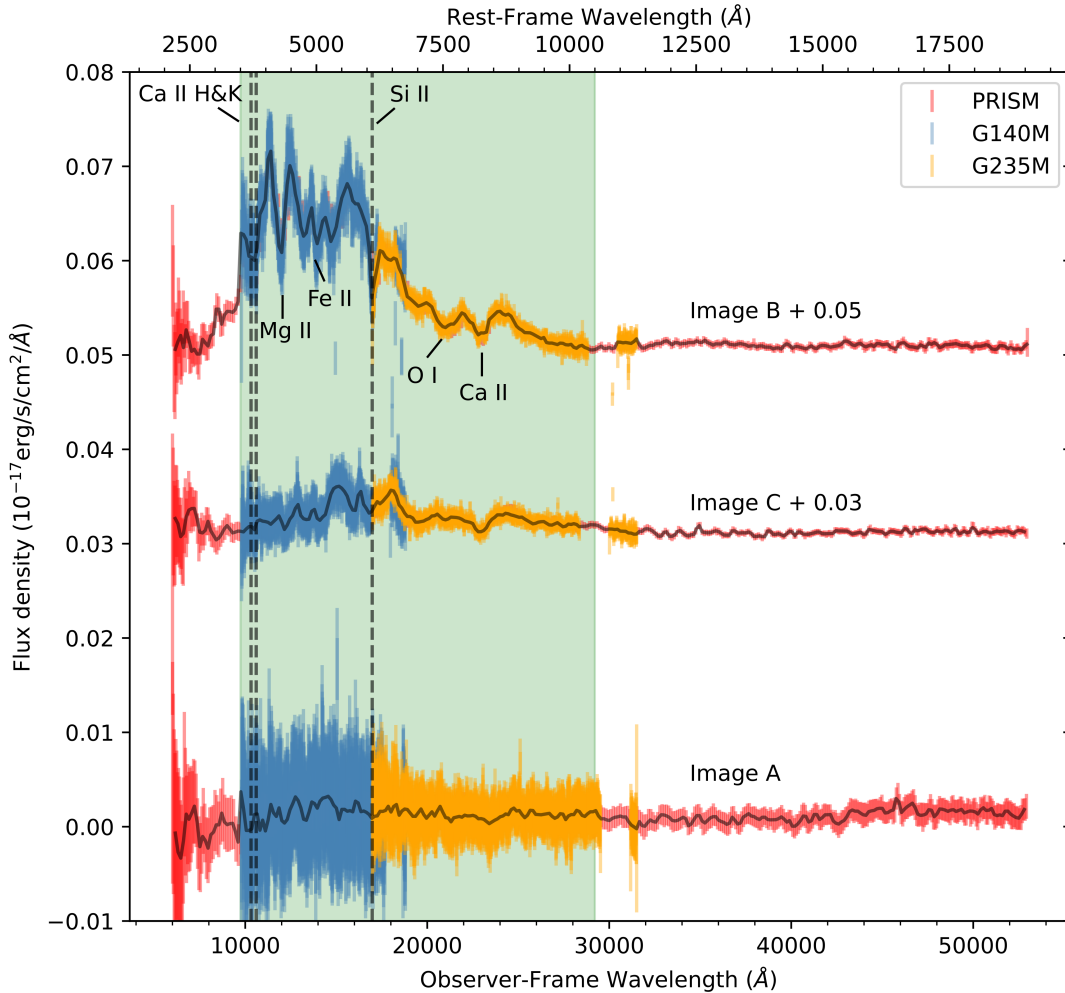


**Figure 4.** NIRSpec spectra of all three images of SN H0pe. Spectra are offset vertically as labeled for clarity. Error bars, merging into color bands as indicated in the legend, show the G140M, G235M, and PRISM spectra. Solid lines show the smoothed spectra using a  $120\text{\AA}$  rolling window. Wavelengths are marked in the observed frame (bottom) and the rest frame (top, based on the host-galaxy  $z = 1.7825$ ). The green shading marks the wavelength range used to match the SN templates and measure the image phases. Dashed vertical lines mark the wavelengths of key absorption features. Spectra are plotted as extracted in a single slitlet, not corrected for slit losses.

galaxy redshift of  $z = 1.7825$ . From Image B, we measured an equivalent width of the Si II  $\lambda 6355$  absorption lines of  $56 \pm 8\text{\AA}$  in the rest frame of the SN. Given the SN Image B phase of  $6.5^{+2.4}_{-1.8}$  d (Section 5), the Si II velocity and its equivalent width are consistent with those of a normal-velocity SN Ia or a SN 1991T-like SN Ia (e.g., Wang et al. 2013; Zhao et al. 2021).

## 5. METHODS OF MEASURING PHASES OF THE SN IMAGES

We employ three methods to constrain the phases (defined as rest-frame days after peak  $B$ -band brightness) of the SN images. The first method is fitting the Hsiao07

(Hsiao et al. 2007) spectral templates to the NIRSpec data using Markov-chain Monte Carlo (MCMC) sampling. Hsiao’s templates were constructed from a library of  $\sim 600$  spectra of  $\sim 100$  SNe Ia. The second method is similar except that the fitting instead uses the SALT3-NIR (Pierel et al. 2022) spectral SN Ia models. The original SALT3 model (Kenworthy et al. 2021) was developed from  $\sim 1200$  spectra of 380 distinct SNe Ia. To create the SALT3-NIR model, an additional 166 SNe Ia with near-infrared data were incorporated, extending the model’s reach to  $2\text{\mu m}$ . The third method is to apply the Supernova Identification (SNID) software package (Blondin & Tonry 2007), which cross-correlates an

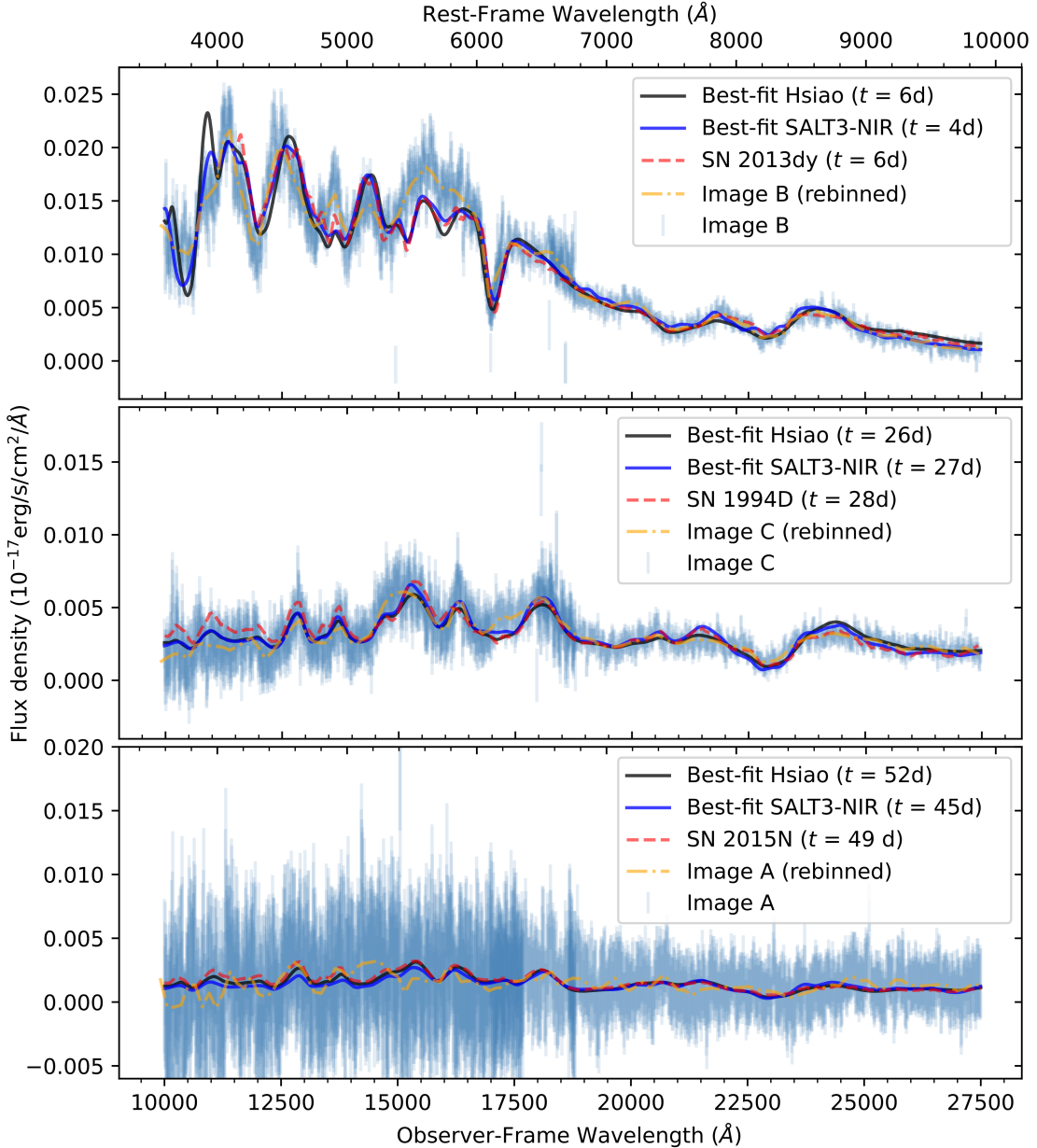


**Figure 5.** Best-fit templates and phases for the three images of SN H0pe as shown in the legends. Thin blue lines, merging into color bands, show  $1\sigma$  error bars. Dash-dotted orange lines show the observed spectra rebinned into a  $120\text{ \AA}$  rolling window. Solid black lines show the best-fit Hsiao07 spectra. Solid blue lines show the best-fit SALT3-NIR model at each phase. Red dashed lines show spectra of previously observed SNe Ia that most closely match the observed spectra of SN H0pe from our NGSF analysis.

observed spectrum with template SN spectra. The SNID approach, in contrast to the others, removes the continuum, and the correlation reflects the features of the spectrum as opposed to the overall shape of the spectral energy distribution. The details of the three analyses are described below, and Appendix B presents the constraints on the phases of the SN images from these analyses, before accounting for systematic uncertainties described in Section 6.

All of constraints on the phases were obtained while the authors were blind to those obtained from fitting the images’ light curves (Pierel et al. 2024, submitted). Therefore the analysis presented herein is entirely independent of the light curve phases. Only after completion of both analyses were the two sets of results unblinded by a third party and an inference for  $H_0$  made (Pierel et al. 2024, submitted).



**Table 2. SN templates that fit the observed spectra.**

Template	Type	Subtype	Phase	$A_V$	$\chi^2_\nu$
<b>Image B</b>					
SN 2013dy	Ia	Ia-norm	6.2	0.4	1.71
SN 2012cg	Ia	Ia-norm	9.6	0.0	2.18
SN 2000cx	Ia	Ia-pec	0.4	0.0	2.60
SN 2013dy	Ia	Ia-norm	0.0	0.0	2.70
SN 2012fr	Ia	Ia-norm	2.3	1.8	2.77
<b>Image C</b>					
SN 1994D	Ia	Ia-norm	28.6	0.1	0.69
SN 2013dy	Ia	Ia-norm	41.3	1.3	0.76
SN 2012cg	Ia	Ia-norm	38.6	0.8	0.77
SN 1991T	Ia	Ia 91T-like	40.0	0.6	0.78
SN 2011by	Ia	Ia-norm	30.3	0.3	0.79

NOTE—Columns show template names, types, subtypes, phases (rest-frame days after peak brightness) for image B or C as indicated, host extinction  $A_V$ , and reduced chi-square of the fit to the SN H0pe spectrum. Rows show the five best-match SN templates from the NGSF analysis.

### 5.1. Hsiao07 SN Ia spectral template

We fit the spectra of the three SN images simultaneously with a shared set of parameters. The fit includes a total of eleven free parameters: the overall normalization  $\alpha$ ; the dust-extinction parameters  $E(B-V)$  and  $R_V$ ; the pair of flux ratios between Images A and B ( $f_A/f_B$ ) and between Images A and C ( $f_A/f_C$ ); the image phases  $t_A$ ,  $t_B$ , and  $t_C$  at the time of observation; and a free background value for each of the three spectra. We use the `emcee` software package (Foreman-Mackey et al. 2013) to sample the model parameters and the implementation of the Hsiao07 template in the `SNCosmo` package (Barbary et al. 2023). As a test, we also fit the Hsiao07 template to each SN spectrum separately. Each of these fits had four model parameters:  $\alpha$ ,  $E(B-V)$ ,  $R_V$ , and  $t_i$ , where  $t_i$  is the phase of that image. These results are also listed in Table B1 and are consistent with the shared-parameter results. Table B1 gives the derived phases, and the black curves in Figure 5 show the best fits. The posterior distributions of the fitted parameters are shown in Figure 6, and Figure 7 illustrates the fit uncertainties.

In the SN spectrum of Image B, as shown in Figures 5 and 7, the most notable deviation between the observed data and the best-fit model occurs in the rest-frame wavelength range of 5 500–6 000 Å. This discrepancy could be attributed to the diversity in the continuum level of SNe Ia near the Si II  $\lambda$ 5972 feature or potentially to incomplete modeling of magnesium and sodium features during host-galaxy subtraction. The

latter might suggest a color gradient within the host galaxy of SN H0pe. Given that our current extraction technique does not account for the color gradient of extended sources, we anticipate that future spectroscopic observations of the host galaxy, conducted in the absence of the SN, will provide insights into this observed discrepancy.

### 5.2. SALT3-NIR model

For the SALT3-NIR (Pierel et al. 2022) analysis, the input parameters for this model are the overall normalization  $x_0$ , a light-curve shape parameter (“stretch”)  $x_1$ , a color parameter  $c$ , and the phase and background parameters as for the analysis using the Hsiao07 template. Because the SALT3-NIR model is limited to phases  $\leq 50$  days, for larger phases, we assigned likelihoods equal to the 50-day value. As for the Hsiao07 templates, we tested independent fits to each spectrum in addition to the primary simultaneous fit to all three spectra. Figure 5 shows the best fits of the SALT3-NIR model to the spectra, and Table B1 lists the best-fit image phases. Appendix C presents the full results of the SALT3-NIR model-fitting including parameter distributions and uncertainties.

The SALT3-NIR results are statistically consistent with those from the Hsiao07-template analysis. However, the phase of Image A from the SALT3-NIR fitting approaches the 50-day upper validity limit of the model. For the joint fitting, this proximity to the limit of the model may affect the SALT3-NIR model’s constraints on the other image phases, potentially leading to biased estimates of the time delays and magnifications. Therefore, we do not rely on the joint SALT3-NIR fitting for our primary constraints on the phases or relative time delays of the images.

### 5.3. SNID

As a third measurement, we derive constraints *independent* of the SN color, i.e., using only the spectral features. For this, we employed SNID (Blondin & Tonry 2007), which removes the continuum from the SN spectrum before cross-correlating the SN spectrum with template spectra. We used both the built-in SNID template library (“template 2.0”) and a library that we constructed from the SALT3-NIR SN Ia template, which includes 1 750 spectra across 70 SN phases, each spanning 25 different combinations of the stretch ( $x_1$ ) and color ( $c$ ) parameters. Figure 8 plots the continuum-removed spectra of Images B and C superimposed on the 100 best-fitting SN spectra.

With SNID’s default template-matching thresholds, 176 templates—all SN Ia—match the Image B spectrum. The matching templates all have early phases

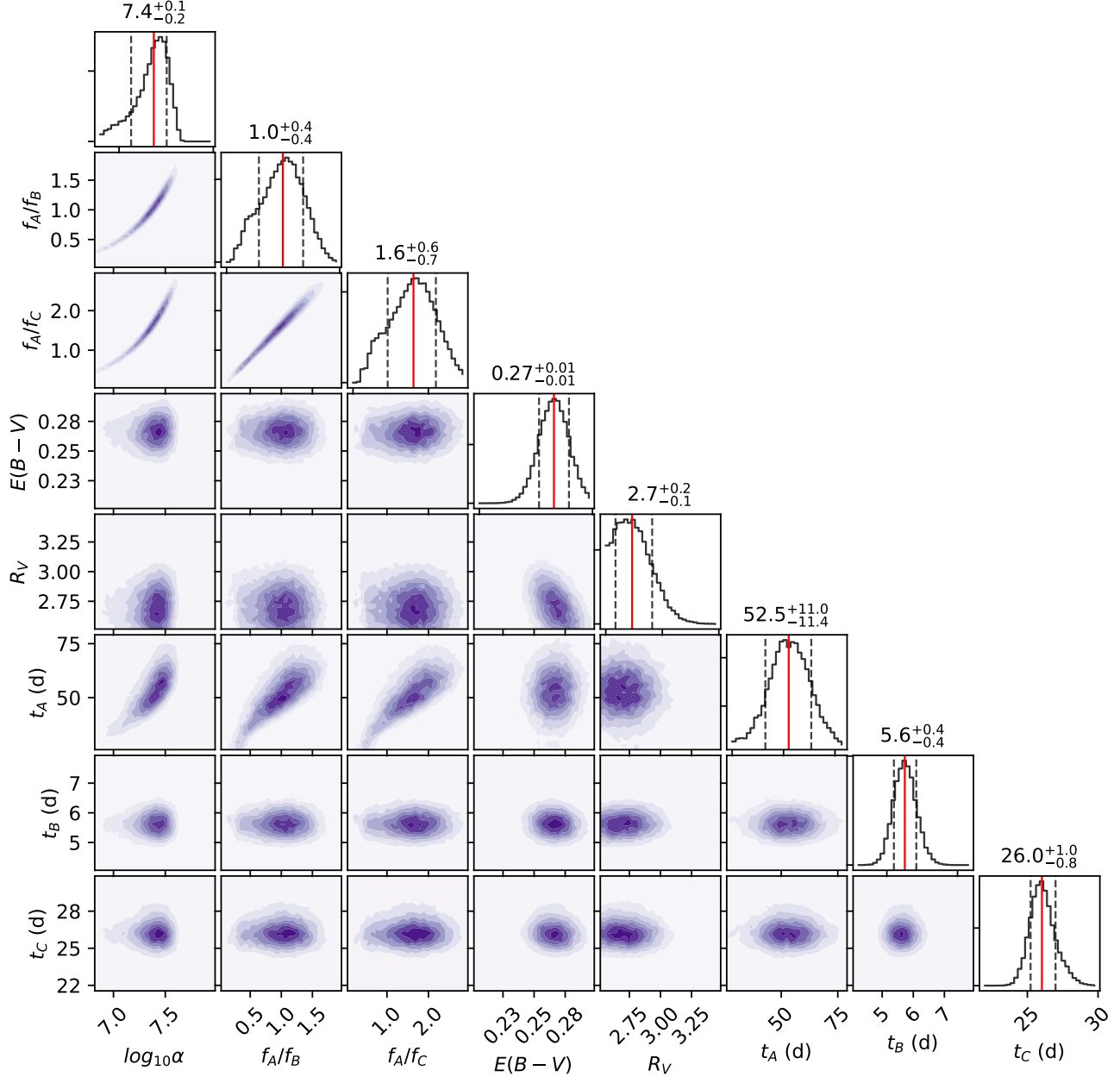


**Figure 6.** Parameter distributions from the Hsiao07 template fits.  $\alpha$ ,  $R_V$ , and  $E(B - V)$  are model parameters (Section 5.1),  $f_A/f_B$  and  $f_A/f_C$  are template-flux ratios between Images A and B and between Images A and C, respectively, and  $t_A$ ,  $t_B$ , and  $t_C$  are rest-frame phases of Images A, B, and C, respectively. The solid vertical line on each histogram marks the median of the parameter, while the dashed vertical lines denote the 68% confidence interval of each distribution.

(Table B1) but are consistent with the Hsiao07 and SALT3-NIR results within the uncertainties (Table B1). There are 163 matching templates that are in the Ia-norm subtype, all giving essentially the same phases but uncertainties larger than those from Hsiao07 or SALT3-NIR. The Image C spectrum has 165 matching templates, 164 of them SNe Ia, and 107 with Ia-norm templates. No phase or even a favored SN type can be iden-

tified from the low signal-to-noise spectrum of Image A. Using the simulated templates generated from the SALT3-NIR model gives phases and uncertainties similar to those from the templates 2.0 package but with a preference for a slightly later phase for Image B (Table B1).

The SNID analysis provides decisive evidence that SN H0pe is Type Ia. All SN phases from the SNID analysis

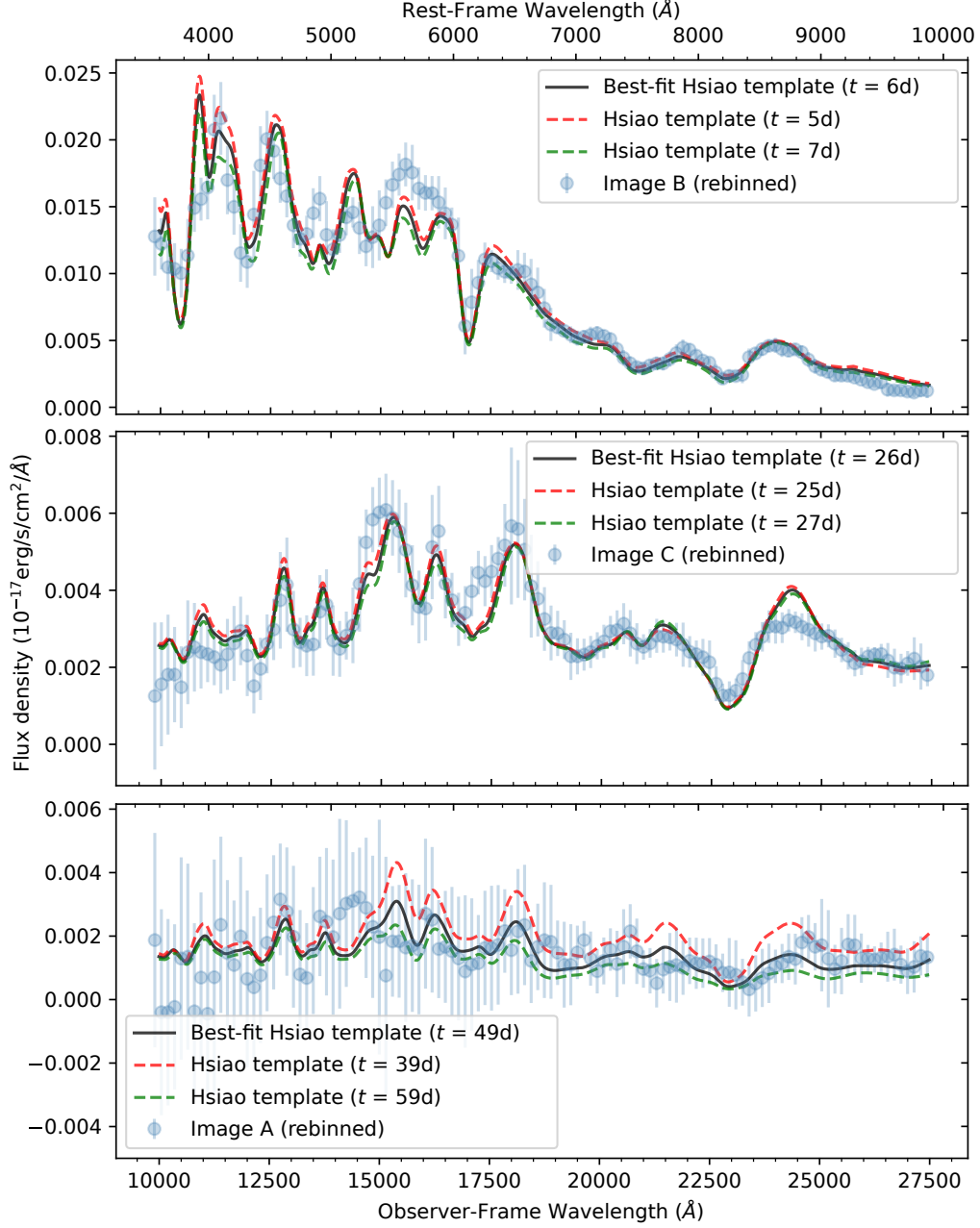


**Figure 7.** Best-fit Hsiao07 templates from Figure 5 are depicted again here, including the models for SN phases that deviate by  $\pm 1\sigma$  (rounded to the nearest integers) from the best-fit phases. Data points and error bars show the observed (rebinned to  $120 \text{ \AA}$ ) SN H0pe spectra.

are consistent with the values from the SALT3-NIR and Hsiao07 analyses.

## 6. UNCERTAINTIES OF THE MEASUREMENT OF TIME DELAYS AND MAGNIFICATIONS

Image A might be at a phase outside the SALT3-NIR model’s valid range, and the image is too faint for SNID to reliably infer its phase. This leaves the Hsiao07 templates as the principal basis for our analysis. To assess the templates’ ability to determine SN phases, our anal-

ysis began with joint fitting of a set of well-observed, nearby SNe Ia with the Hsiao07 templates, as described in Section 6.1. Section 6.2 presents the subsequent modeling of the effects of millilensing and microlensing to assess those processes’ impacts on the time delay and magnification measurements. Final constraints on the SN phases, magnifications, and relative time delays are presented in Section 7.

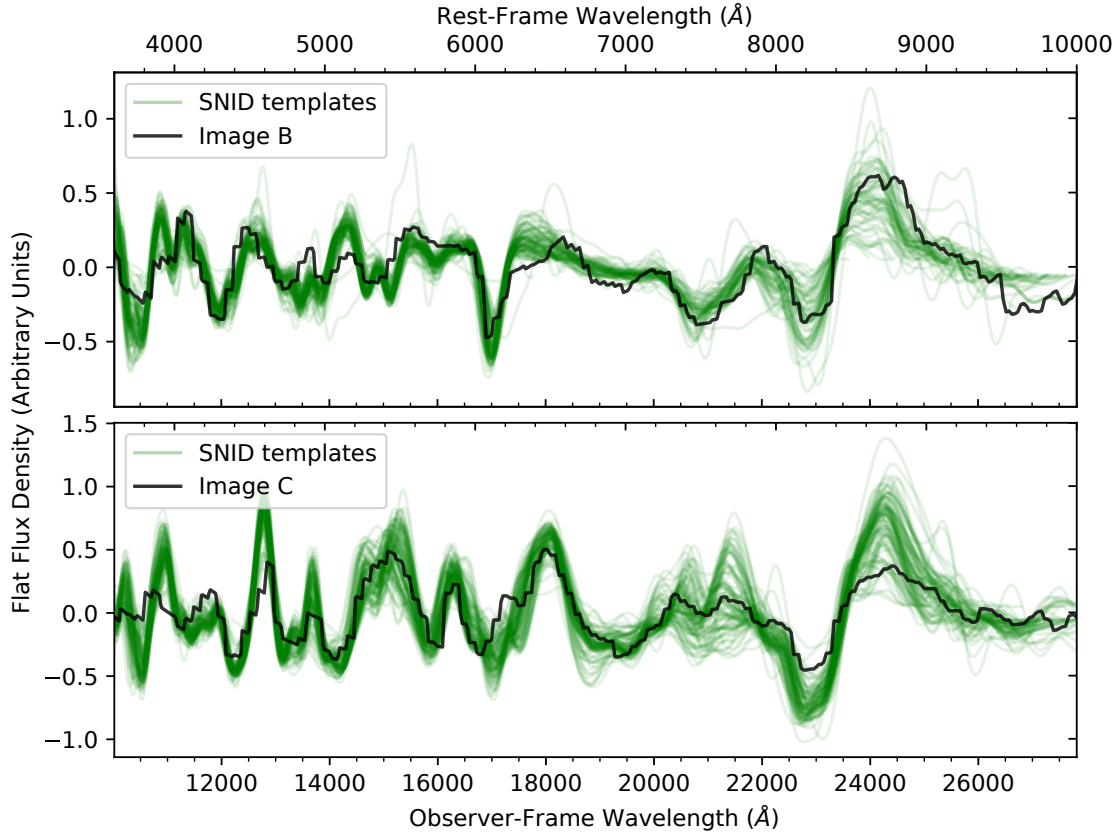


**Figure 8.** Flattened flux density of SN Images B and C for the SNID analysis (black). Green curves show the 100 best-fitting SNID templates.

### 6.1. Simulation of the Hsiao07 modeling

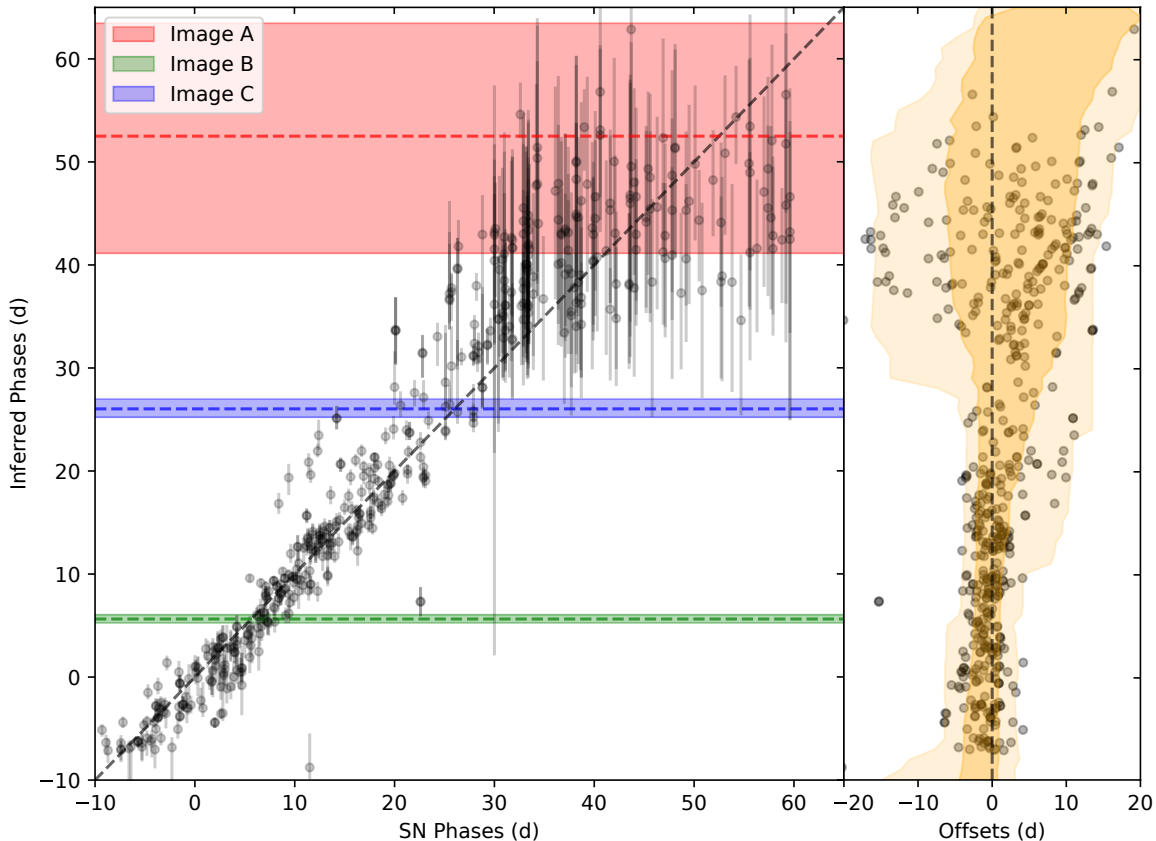
To assess the ability of the Hsiao07 template to recover the phase of the SN images, we applied the same analysis to the spectra of a set of well-observed, nearby SNe Ia listed in SNID’s built-in library. The SNe were chosen to have at least one spectrum in each of the following ranges of phase relative to maximum:  $(-10, 10)$ ,  $(10, 30)$ , and  $(30, 60)$  days. These ranges correspond to the values inferred for SN H0pe Images B, C, and A, respectively, using the Hsiao07 template, which includes spectra through 80 days. This gave 228 sets of spectra for the simulation with each set consisting of three SN spectra in the three phase bins. To each spectrum, we added the residuals of the NIRSpc spectra from the smoothed spectra (as shown by the dash-dotted lines in Figure 5), drawing randomly from the residual distribution across all wavelengths. This step assumes the residuals are random rather than correlated with wavelength. Additionally, we rescaled the spectra to match the signal-to-noise ratio of the NIRSpc observations.

Figure 9 compares the actual and inferred phases. The residuals and the confidence intervals, shown by shaded areas, are plotted in the right panels of Figure 9. As

shown in Figure 9, the inferred phase is generally in agreement with the true value, and the agreement is especially good at phases  $< 30$  days. Beyond 30 days, the uncertainty associated with the inferred phase is significantly greater, primarily because of Image A’s low signal-to-noise ratio and the slow evolution of SN spectral features at these phases.

### 6.2. Millilensing and microlensing

Lens-model predictions of the image magnification ratios and relative time delays include only structure on the scale of galaxy members and the cluster itself. Therefore, the effects of millilensing by subhalos and microlensing by stars and compact objects have to be included in the uncertainties on the inferred phases and time delays. Millilenses affect only the magnifications of the SN images because the SN photosphere ( $\sim 10^{14}$  to  $10^{15}$  cm in radius) is much smaller than the scale of a millilens caustic. Microlenses, such as stars and stellar remnants, on the other hand, have Einstein radii comparable to the size of the SN photosphere. As the expanding SN photosphere crosses microlens caustics, different portions of the photosphere can be magnified differently, leading to wavelength-dependent changes in



**Figure 9.** **Left:** inferred phases from Hsiao07 fitting versus actual phases of a set of nearby SNe Ia. Error bars correspond to the 68% confidence intervals of the inferred phases. Horizontal dashed lines and shaded regions mark the inferred phases and their 68% confidence intervals for the three images of SN H0pe. The diagonal dashed line shows equality. **Right:** deviation of the best-fit inferred phase from the actual phase. Shaded regions mark the 68% (darker) and 95% (lighter) confidence intervals of the residuals measured within a 10-day rolling window. Simulations including input SNe beyond 60 days could, in principle, increase the uncertainty for Image A, and constraints will benefit from future simultaneous measurement from spectra and imaging.

the SN spectrum (Goldstein et al. 2018; Foxley-Marrable et al. 2018; Huber et al. 2019). Consequently, microlensing can affect not only the magnification of the SN images but also time-delay estimates.

To compute the uncertainties due to microlensing and millilensing, we utilized 4 000 simulations of SNe Ia spectra. (The simulations are described in detail in the companion paper presenting time-delay inferences from the photometry of the SN: Pierel et al. 2024, submitted.) In brief, for each of the four theoretical models of microlensing caustics from Suyu et al. (2020) and Huber et al. (2021), a set of SNe Ia were placed at 1 000 random positions in the source plane. The simulated spectrum at each position compared to the input spectrum without microlensing was used to determine the wavelength-dependent magnification due to microlensing. The millilens magnification distributions were calculated for a range of dark-matter subhalo mass functions and substructure fractions anticipated from theory

as well as observations (Gilman et al. 2020). A magnification drawn from one of the millilensing distributions was applied to each simulated SN sight line. As in Section 6.1, we added noise to the simulated spectra to match the signal-to-noise ratios of the three SN H0pe spectra. Then we simultaneously fit the set of three simulated spectra corresponding to the three SN H0pe images. The differences between the inferred and input SN phases and magnifications yielded an estimate of the systematic uncertainties arising from millilensing and microlensing. Table 3 gives the results.

## 7. CONSTRAINTS ON TIME DELAYS AND MAGNIFICATIONS

For our joint fitting using the Hsiao07 template, for each  $i$ -th step in the MCMC chain from our joint fitting, we obtained a set of eight model parameters, denoted as  $\mathbf{X}^i = [\alpha_A^i, \alpha_B^i, \alpha_C^i, E(B - V)^i, R_V^i, t_A^i, t_B^i, t_C^i]$ . The alphas are related to the ones described in Section 5.1

**Table 3.** Microlensing and Millilensing Uncertainties

$\sigma_m$ ( $\pm$ AB magnitude)	Image A	Image B	Image C
Microlensing	0.04	0.12	0.04
Millilensing	0.04	0.04	0.04

NOTE—Median standard deviation of magnitude changes  $\sigma_m$  across the rest-frame wavelength range 3 600 Å to 10 000 Å in the simulated SN Ia sample.

by  $\alpha_A^i = \alpha^i$ ,  $\alpha_B^i = \alpha^i/(f_A/f_B)^i$ ,  $\alpha_C^i = \alpha^i/(f_A/f_C)^i$ . We proceeded by randomly selecting an SN among the SNe Ia with inferred phase within a  $\pm 10$ -day window and calculating the median offsets of this SN’s inferred phase from its actual value. Next, we chose a set of three SN spectra from our simulated millilensing and microlensing samples and determined the median offsets between the input and inferred parameter values. These offsets, derived from the simulations, were then applied to the parameters in the MCMC chain. This process resulted in a modified set of eight parameters  $\mathbf{Y}^i$ , where  $Y_1^i = \alpha_A^i + \delta\alpha_A^j + \delta\alpha_A^k$ ,  $Y_2^i = \alpha_B^i + \delta\alpha_B^j + \delta\alpha_B^k$ ,  $Y_3^i = \alpha_C^i + \delta\alpha_C^j + \delta\alpha_C^k$ ,  $Y_4^i = E(B - V)^i + \delta E(B - V)^k$ ,  $Y_5^i = R_V^i + \delta R_V^k$ ,  $Y_6^i = t_A^i + \delta t_A^j + \delta t_A^k$ ,  $Y_7^i = t_B^i + \delta t_B^j + \delta t_B^k$  and  $Y_8^i = t_C^i + \delta t_C^j + \delta t_C^k$ . Here the  $j$  and  $k$  indices are for the set of randomly selected SN spectra from the low-redshift SN Ia simulation and from the millilensing and microlensing simulation, respectively. For the simulation of the low-redshift SNe Ia, we assume that the extinction parameters  $R_V$  and  $E(B - V)$  were fit accurately for each SN.

To constrain the absolute magnifications of the three images of the SN, we used the MCMC sample from our joint fitting. For each set of modified model parameters  $\mathbf{Y}^i$  in the MCMC chain at the  $i$ -th step, we generated a set of three synthetic SN spectra using the `SNCosmo` package (Barbary et al. 2023).

The expected rest-frame  $B$ -band magnitudes of SNe Ia were obtained from the complete sample of Scolnic et al. (2018). To estimate  $\hat{m}_B$  at  $z = 1.782$  independent of the cosmological distance and  $H_0$ , we used a polynomial fit to interpolate  $\hat{m}_B$  as a function of the logarithmic redshift, which yields  $\hat{m}_B = 26.32 \pm 0.03$  at  $z = 1.782$ . As a cross-check performed after unblinding, a concordance cosmology described by the  $\Lambda$  cold dark matter model ( $\Lambda$ CDM) with  $\Omega_m = 0.3$ ,  $\Omega_\Lambda = 0.7$ , and a Hubble constant  $H_0 = 70 \text{ km s}^{-1} \text{ Mpc}^{-1}$  yields  $\hat{m}_B = 26.30$  at the redshift.

The magnitude in a specific band for a given amplitude of the model is dependent upon host-galaxy extinction. In our analysis using the Hsiao07 templates, we assumed that SN H0pe is a standard candle in the

**Table 4.**  $Y$ -band apparent AB magnitudes of the SN images.

$i =$	A	B	C
Magnitudes from Hsiao07 fits			
	$25.41^{+0.45}_{-0.32}$	$24.60^{+0.05}_{-0.05}$	$24.84^{+0.06}_{-0.06}$
Predicted magnitudes for $t_i = 0$			
	$24.39^{+0.69}_{-0.63}$	$24.18^{+0.22}_{-0.48}$	$24.85^{+0.29}_{-0.21}$

NOTE—The rest-frame  $Y$ -band photometry was synthesized using the Dark Energy Camera’s  $y$  filter (Abbott et al. 2018) set at airmass 1.3 based on the Hsiao07-template fits. Phases  $t_i$  are rest-frame days after the peak brightness in the rest-frame  $B$ -band.

rest-frame  $Y$ -band, where previous studies (e.g., Avelino et al. 2019) show that the SN brightness is not substantially correlated with the spectral stretch and color and is homogeneous without these corrections. We then determined the expected  $Y$ -band magnitude for an unmagnified SN Ia. For an SN Ia spectrum produced by the Hsiao07 template with the best-fit dust-extinction parameters, we varied the normalization factor of the spectrum to match its  $Y$ -band magnitude to that of an SN Ia without extinction and with a rest-frame  $B$ -band magnitude ( $\hat{m}_B$ ) equal to the expected value. This yielded an unlensed  $Y$ -band magnitude of  $27.15 \pm 0.03$ . Subsequently, we synthesized a  $Y$ -band measurement of the SN for each set of parameters  $\mathbf{Y}^i$  in the MCMC chain and calculated the predicted  $Y$ -band magnitude at the SN phase  $t = 0$  for each image based on the Hsiao07 template. We then determined the magnification by comparing the resultant  $Y$ -band magnitude to the expected value. Table 4 list the resultant  $Y$ -band magnitudes derived from the MCMC chain and the predicted magnitudes at  $t = 0$ .

Finally, we reconstructed the posterior distribution of the time delays and the macro lens magnifications (i.e., the magnifications from the cluster lens) as illustrated in Figure 10. Table 5 lists the correlation matrices of the relative time delays, magnification ratios, and magnifications from our analysis using the Hsiao07 template. Our final constraints on the SN phases, relative time delays, and magnifications are listed in Table 6.

## 8. A POST-UNBLINDING TEST

As described in Section 6.1, we chose three bins in SN phase to select the spectra of nearby SNe Ia. These bins were determined *a priori* based on the result of the joint MCMC fitting, before we conducted the simulation. Given the low signal-to-noise ratio of Image A’s spectrum, there is a lack of sensitivity to phases for SN

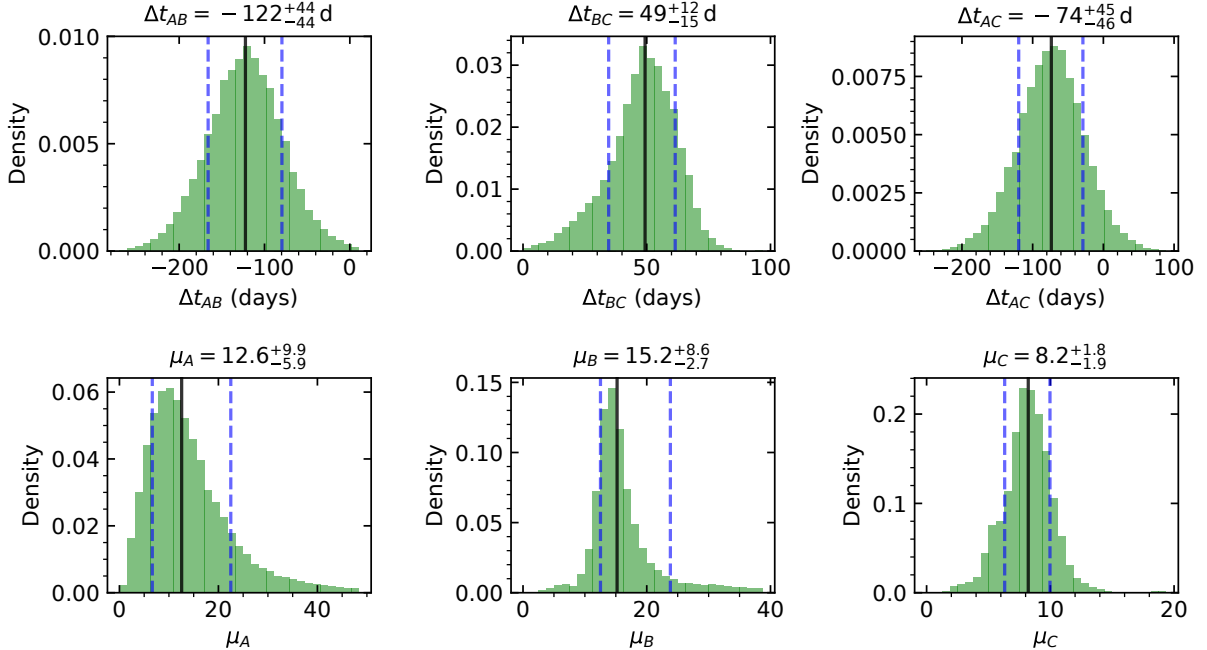


**Figure 10.** Posterior probability densities of the relative time delays and the macro lens magnifications between SN H0pe’s images. Histograms show values derived from the Hsiao07 templates. The distributions integrate the uncertainty from the MCMC fitting with systematic uncertainties, estimated from the model fitting of nearby SN Ia spectra and from the simulated SN Ia spectra. The uncertainties take into account the impacts of microlensing and millilensing effects.

Ia spectra with inferred phases beyond  $\sim 40$  days. To assess the impact of the upper limit of the third phase bin (assigned for Image A) on the inferred time delays and magnifications, we expanded the range of third phase bin from (30, 60) days to (30, 80) days. We then performed the same simulation as described in Section 6.1 with the extended phase bin, while keeping the results of other simulations unchanged to determine the final constraints. Table 6 lists the resulting constraints on the phases, the relative time delays, and the magnifications of SN H0pe’s images. Figure 11 shows the distributions of these parameters, over-plotted on the pre-unblinding distributions. This test was conducted after the unblinding of the result from the  $H_0$ -inference team (Pascale et al. 2024, in prep.).

As shown in Figure 11, the distributions of relative time delays and magnifications remain largely unaffected by the adjustment of the upper limit, for which the deviations of the corresponding distributions are much smaller compared to the uncertainties of these measurements. Given the slightly longer time delays compared to the original result, the inferred  $H_0$  will be  $\sim 3\%$  smaller than that based on the pre-unblinding constraints. However, the difference is only  $\sim 0.1\sigma$ , which is not statistically substantial. For the  $H_0$  inference by Pascale et al. 2024 based on the time-delay measurements from both the spectroscopic and photo-

metric analyses, the impact of the upper limit of the phase bin for our simulation is minimal ( $< 1\%$ ).

## 9. CONCLUSIONS

All of our analyses of the spectra of SN H0pe classify SN H0pe as a Type Ia SN and favor a “normal” (Blondin & Tonry 2007) subtype. The velocity of the Si II  $\lambda 6355$  absorption line is consistent with a normal-velocity SN Ia. The SN phases and relative time delays are constrained with  $1\text{-}\sigma$  uncertainties of 2-4 days for Images B and C and two weeks for the latest-arriving Image A.

Our analyses using the Hsiao07 template, the SALT3-NIR model, and the SNID software package yield consistent results for the phases of the SN images. The relative time delays between the three SN H0pe images and their magnifications, as derived from our analyses based on the Hsiao07 template and the SALT3-NIR model, are statistically in agreement. However, the inferred phase of Image A is near or above the upper boundary of the SALT3-NIR model’s valid range. During the joint fitting, this affected the constraints of the SALT3-NIR model, potentially biasing the estimates of time delays and magnifications. The SNID model approach, which was unable to utilize the information from the faintest Image A, yielded larger uncertainties than the Hsiao07 analysis but only uses the spectral features, since the SN continuum is subtracted.

**Table 5. Correlation matrices of model parameters**

	$\Delta t_{AB}$	$\Delta t_{BC}$	$\Delta t_{AC}$	$\mu_A/\mu_B$	$\mu_B/\mu_C$	$\mu_A/\mu_C$	$\mu_A$	$\mu_B$	$\mu_C$
Hsiao07									
$\Delta t_{AB}$	1.000								
$\Delta t_{BC}$	-0.002	1.000							
$\Delta t_{AC}$	0.947	0.320	1.000						
$\mu_A/\mu_B$	-0.572	0.086	-0.514	1.000					
$\mu_B/\mu_C$	-0.268	-0.457	-0.402	-0.178	1.000				
$\mu_A/\mu_C$	-0.633	-0.304	-0.698	0.420	0.678	1.000			
$\mu_A$	-0.721	-0.131	-0.725	0.480	0.525	0.872	1.000		
$\mu_B$	-0.322	-0.223	-0.394	-0.202	0.851	0.535	0.622	1.000	
$\mu_C$	-0.020	0.651	0.191	0.009	-0.800	-0.321	0.021	0.022	1.000
SALT3-NIR									
$\Delta t_{AB}$	1.000								
$\Delta t_{BC}$	-0.082	1.000							
$\Delta t_{AC}$	0.932	0.284	1.000						
$\mu_A/\mu_B$	-0.467	0.065	-0.426	1.000					
$\mu_B/\mu_C$	-0.055	-0.243	-0.141	-0.409	1.000				
$\mu_A/\mu_C$	-0.516	-0.244	-0.585	0.516	0.317	1.000			
$\mu_A$	-0.639	-0.030	-0.626	0.683	0.101	0.797	1.000		
$\mu_B$	-0.053	-0.120	-0.095	-0.477	0.898	0.127	0.112	1.000	
$\mu_C$	0.018	0.588	0.231	0.014	-0.357	-0.458	0.001	-0.070	1.000

NOTE—Each  $i$ -th row and  $j$ -th column is the correlation between  $i$ -th and  $j$ -th parameters. The upper section of the table is for the Hsiao07 models (Section 5.1), and the lower section is for the SALT3-NIR models (Section 5.2). Parameters are the relative time delays  $\Delta t_{AB}$ ,  $\Delta t_{BC}$ ,  $\Delta t_{AC}$ , the magnification ratios  $\mu_A/\mu_B$ ,  $\mu_B/\mu_C$ ,  $\mu_A/\mu_C$ , and the magnifications  $\mu_A$ ,  $\mu_B$ ,  $\mu_C$ .

In addition to time delays and magnifications, the fits using the Hsiao07 template constrain the host extinction  $E(B-V) = 0.27 \pm 0.02$  and  $R_V = 2.73 \pm 0.17$ . The  $E(B-V)$  is consistent with the values listed in Table 4 of Frye et al. (2024). This indicates that the SN exploded in a relatively dusty environment with an extinction  $A_V \gtrsim 0.7$ .

SN H0pe will be valuable not only for measuring the Hubble–Lemaître constant but also, because this is the second-highest currently known redshift SN Ia, for testing whether SNe at large lookback times had the same properties as SNe today. Based on spectra at multiple rest-frame epochs, SN H0pe matches the most common type of SN Ia in the nearby universe. Our analysis of the SN images’ phases, based solely on the NIRSpec spectra, suggests a relative uncertainty of  $\gtrsim 20\%$  in the time delay between the two brightest images (B and C). This would limit the precision of constraints on the Hubble constant from the measured spectroscopic time delay to be  $\gtrsim 20\%$ , given more precise lens model predictions. Beyond the blind analysis detailed in this paper

and the associated photometric-analysis paper (Pierel et al. 2024, submitted), a comprehensive joint analysis—utilizing both the spectroscopic time delay and the photometric measurements (Pascale et al. 2024, in prep.)—will yield a combined measurement of the Hubble constant with improved precision.



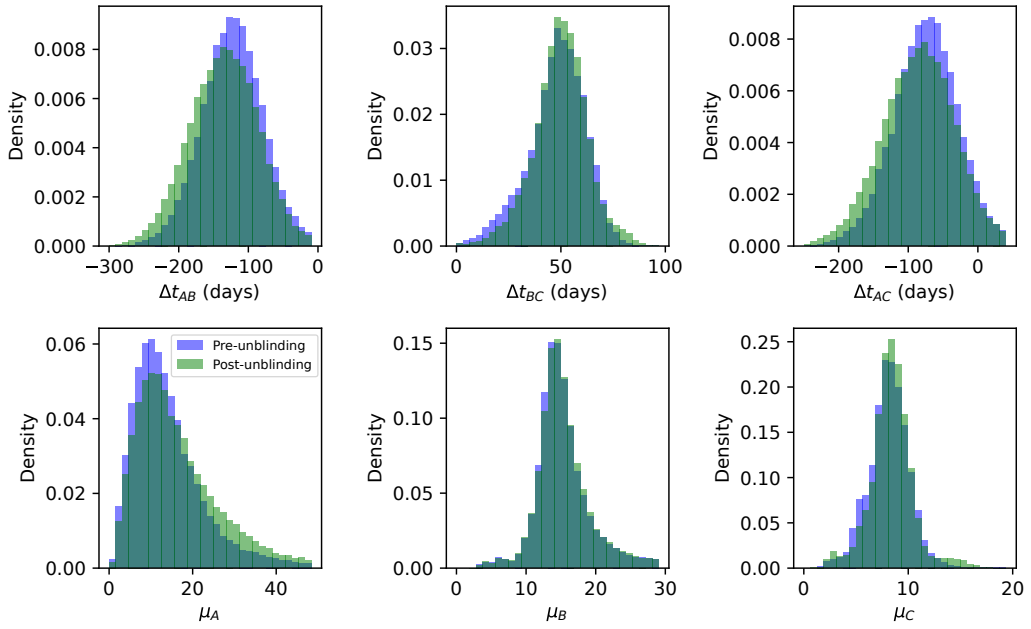


**Figure 11.** Posterior probability densities of the relative time delays and the macro lens' magnifications between SN H0pe's images. For the pre-unblinding result, we simulated the joint Hsiao07-template fitting by selecting a set of three spectra from three SN phase bins:  $(-10, 10)$ ,  $(10, 30)$ , and  $(30, 60)$  days (as described in Section 6.1). For the post-unblinding test, we expand the third phase bin to  $(30, 80)$  days.

**Table 6. Summary of final constraints.**

$i =$	A	B	C
Hsiao07 template fits			
$t_i$	$50.6^{+16.1}_{-15.3}$ d	$6.5^{+2.4}_{-1.8}$ d	$24.3^{+3.9}_{-3.9}$ d
$t_i$	$54.5^{+18.7}_{-17.0}$ d	$6.2^{+2.5}_{-1.7}$ d	$24.5^{+3.6}_{-3.4}$ d
$\mu_i$	$12.6^{+9.9}_{-5.9}$	$15.2^{+8.6}_{-2.7}$	$8.2^{+1.8}_{-1.9}$
$\mu_i$	$14.5^{+13.3}_{-7.1}$	$15.3^{+8.2}_{-2.7}$	$8.4^{+1.7}_{-1.7}$
SALT3-NIR fits			
$t_i$	$42.8^{+11.4}_{-9.7}$ d	$5.6^{+2.3}_{-2.1}$ d	$26.7^{+2.5}_{-4.2}$ d
$\mu_i$	$9.3^{+5.2}_{-3.7}$	$16.2^{+11.3}_{-3.2}$	$10.3^{+1.7}_{-2.0}$
$\mu_i$	$9.0^{+4.8}_{-3.6}$	$15.6^{+11.1}_{-3.0}$	$9.8^{+1.6}_{-2.0}$
$i =$	AB	BC	AC
Hsiao07 template fits			
$\Delta t_i$	$-122.3^{+43.7}_{-43.8}$ d	$49.3^{+12.2}_{-14.7}$ d	$-73.6^{+44.7}_{-46.1}$ d
$\Delta t_i$	$-133.8^{+47.2}_{-51.1}$ d	$50.3^{+12.0}_{-12.7}$ d	$-82.8^{+50.2}_{-54.6}$ d
SALT3-NIR fits			
$\Delta t_i$	$-103.6^{+27.9}_{-32.2}$ d	$57.7^{+10.2}_{-12.3}$ d	$-46.8^{+29.5}_{-33.7}$ d

NOTE—Phases  $t_i$  are rest-frame days after the peak brightness. Magnifications  $\mu_i$  are the macro-magnifications from the cluster and are based on SN Ia absolute magnitudes as described in Section 7 for the Hsiao07 templates and Section C.3 for the SALT3-NIR fits. For the Hsiao07 template fits, the second row of  $t_i$ ,  $\mu_i$ , and  $\Delta t_i$  are based on a post-unblinding test where we expand the third phase bin for selecting the nearby SN Ia spectra from (30, 60) days to (30, 80) days (as described in Section 8). For the SALT3-NIR fits, the first row of  $\mu_i$  is based on  $B$ -band absolute magnitudes, and the second row is based on  $Y$ -band. Relative time delays  $\Delta t_i$  are days in the observer frame.

1 This work is based on observations made with the  
 2 NASA/ESA/CSA *JWST*. The data were obtained from  
 3 the Mikulski Archive for Space Telescopes (MAST) at  
 4 the Space Telescope Science Institute, which is oper-  
 5 ated by the Association of Universities for Research  
 6 in Astronomy, Inc., under NASA contract NAS 5-  
 7 03127 for *JWST*. These observations are associated  
 8 with program *JWST* DDT 4446. RAW and SHC  
 9 acknowledge support from NASA *JWST* Interdisci-  
 10 plinary Scientist grants NAG5-12460, NNX14AN10G  
 11 and 80NSSC18K0200 from GSFC. AZ acknowledges  
 12 support by Grant No. 2020750 from the United States-  
 13 Israel Binational Science Foundation (BSF) and Grant  
 14 No. 2109066 from the United States National Science  
 15 Foundation (NSF); by the Ministry of Science & Tech-  
 16 nology, Israel; and by the Israel Science Foundation  
 17 Grant No. 864/23. SH thanks the Max Planck Society  
 18 for support through the Max Planck Research Group for  
 19 S. H. Suyu and the European Research Council (ERC)  
 20 under the European Union’s Horizon 2020 research and  
 21 innovation programme (grant agreement No 771776) for  
 22 funding. CL acknowledges support from the National  
 23 Science Foundation Graduate Research Fellowship un-  
 24 der grant No. DGE-2233066. P.L.K. acknowledges fund-  
 25 ing from NSF grants AST-1908823 and AST-2308051.

Data used in this paper can be retrieved at MAST:  
 doi: 10.17909/rqdx-3976.

*Facilities:* *JWST* (NIRSpec spectroscopy and NIR-  
 Cam imaging)

*Software:* jwst 1.10.2 (<https://jwst-pipeline.readthedocs.io/en/latest/jwst/introduction.html>),  
 MOS Optimal Spectral Extraction ([https://spacetelescope.github.io/jdat\\_notebooks/notebooks/optimal\\_extraction/Spectral\\_Extraction-static.html](https://spacetelescope.github.io/jdat_notebooks/notebooks/optimal_extraction/Spectral_Extraction-static.html)),  
 sncosmo (<https://sncosmo.readthedocs.io/en/stable/>),  
 emcee (<https://emcee.readthedocs.io/en/stable/>),  
 NGSF (<https://github.com/oyaron/NGSF>), SNID  
 (<https://people.lam.fr/blondin.stephane/software/snid/>).

## REFERENCES

- Abbott, T. M. C., Abdalla, F. B., Allam, S., et al. 2018, The Astrophysical Journal Supplement Series, 239, 18, doi: [10.3847/1538-4365/aae9f0](https://doi.org/10.3847/1538-4365/aae9f0)
- Avelino, A., Friedman, A. S., Mandel, K. S., et al. 2019, The Astrophysical Journal, 887, 106, doi: [10.3847/1538-4357/ab2a16](https://doi.org/10.3847/1538-4357/ab2a16)
- Barbary, K., Bailey, S., Barentsen, G., et al. 2023, SNCosmo, v2.10.1, Zenodo, Zenodo, doi: [10.5281/zenodo.8091892](https://doi.org/10.5281/zenodo.8091892)
- Blondin, S., & Tonry, J. L. 2007, ApJ, 666, 1024, doi: [10.1086/520494](https://doi.org/10.1086/520494)
- Bushouse, H., Eisenhamer, J., Dencheva, N., et al. 2022, JWST Calibration Pipeline, 1.8.2, Zenodo, Zenodo, doi: [10.5281/zenodo.7325378](https://doi.org/10.5281/zenodo.7325378)
- Chen, W., Kelly, P. L., Oguri, M., et al. 2022, Nature, 611, 256, doi: [10.1038/s41586-022-05252-5](https://doi.org/10.1038/s41586-022-05252-5)
- Dhawan, S., Johansson, J., Goobar, A., et al. 2020, MNRAS, 491, 2639, doi: [10.1093/mnras/stz2965](https://doi.org/10.1093/mnras/stz2965)
- Filippenko, A. V. 1997, ARA&A, 35, 309, doi: [10.1146/annurev.astro.35.1.309](https://doi.org/10.1146/annurev.astro.35.1.309)
- Foreman-Mackey, D., Hogg, D. W., Lang, D., & Goodman, J. 2013, PASP, 125, 306, doi: [10.1086/670067](https://doi.org/10.1086/670067)
- Foxley-Marrable, M., Collett, T. E., Vernardos, G., Goldstein, D. A., & Bacon, D. 2018, Monthly Notices of the Royal Astronomical Society, 478, 5081, doi: [10.1093/mnras/sty1346](https://doi.org/10.1093/mnras/sty1346)
- Frye, B., Pascale, M., Cohen, S., et al. 2023, Transient Name Server AstroNote, 96, 1
- Frye, B. L., Pascale, M., Pierel, J., et al. 2024, The Astrophysical Journal, 961, 171, doi: [10.3847/1538-4357/ad1034](https://doi.org/10.3847/1538-4357/ad1034)
- Gilman, D., Birrer, S., Nierenberg, A., et al. 2020, \mnras, 491, 6077, doi: [10.1093/mnras/stz3480](https://doi.org/10.1093/mnras/stz3480)
- Goldstein, D. A., Nugent, P. E., Kasen, D. N., & Collett, T. E. 2018, The Astrophysical Journal, 855, 22, doi: [10.3847/1538-4357/aaa975](https://doi.org/10.3847/1538-4357/aaa975)
- Goldwasser, S., Yaron, O., Sass, A., et al. 2022, Transient Name Server AstroNote, 191, 1
- Goobar, A., Amanullah, R., Kulkarni, S. R., et al. 2017, Science, 356, 291, doi: [10.1126/science.aal2729](https://doi.org/10.1126/science.aal2729)
- Goobar, A., Johansson, J., Schulze, S., et al. 2022, arXiv e-prints, arXiv:2211.00656, doi: [10.48550/arXiv.2211.00656](https://doi.org/10.48550/arXiv.2211.00656)

- Grillo, C., Pagano, L., Rosati, P., & Suyu, S. H. 2024, arXiv e-prints, arXiv:2401.10980, doi: [10.48550/arXiv.2401.10980](https://doi.org/10.48550/arXiv.2401.10980)
- Guy, J., Sullivan, M., Conley, A., et al. 2010, *Astronomy and Astrophysics*, 523, A7, doi: [10.1051/0004-6361/201014468](https://doi.org/10.1051/0004-6361/201014468)
- Horne, K. 1986, *PASP*, 98, 609, doi: [10.1086/131801](https://doi.org/10.1086/131801)
- Hsiao, E. Y., Conley, A., Howell, D. A., et al. 2007, *ApJ*, 663, 1187, doi: [10.1086/518232](https://doi.org/10.1086/518232)
- Huber, S., Suyu, S. H., Noebauer, U. M., et al. 2021, *âp*, 646, A110, doi: [10.1051/0004-6361/202039218](https://doi.org/10.1051/0004-6361/202039218)
- . 2019, *Astronomy & Astrophysics*, 631, A161, doi: [10.1051/0004-6361/201935370](https://doi.org/10.1051/0004-6361/201935370)
- Johansson, J., Goobar, A., Price, S. H., et al. 2021, *MNRAS*, 502, 510, doi: [10.1093/mnras/staa3829](https://doi.org/10.1093/mnras/staa3829)
- Kelly, P. L., Rodney, S. A., Treu, T., et al. 2015, *Science*, 347, 1123, doi: [10.1126/science.aaa3350](https://doi.org/10.1126/science.aaa3350)
- . 2016, *ApJL*, 819, L8, doi: [10.3847/2041-8205/819/1/L8](https://doi.org/10.3847/2041-8205/819/1/L8)
- Kelly, P. L., Rodney, S., Treu, T., et al. 2023, *Science*, 380, eabh1322, doi: [10.1126/science.abh1322](https://doi.org/10.1126/science.abh1322)
- Kelly, P. L., Rodney, S., Treu, T., et al. 2023, *ApJ*, 948, 93, doi: [10.3847/1538-4357/ac4ccb](https://doi.org/10.3847/1538-4357/ac4ccb)
- Kenworthy, W. D., Jones, D. O., Dai, M., et al. 2021, *ApJ*, 923, 265, doi: [10.3847/1538-4357/ac30d8](https://doi.org/10.3847/1538-4357/ac30d8)
- Liu, Y., & Oguri, M. 2024, arXiv e-prints, arXiv:2402.13476, doi: [10.48550/arXiv.2402.13476](https://doi.org/10.48550/arXiv.2402.13476)
- Moffat, A. F. J. 1969, *A&A*, 3, 455
- Newville, M., Otten, R., Nelson, A., et al. 2021, *lmfit/lmfit-py*: 1.0.3, 1.0.3, Zenodo, doi: [10.5281/zenodo.5570790](https://doi.org/10.5281/zenodo.5570790)
- Pierel, J. D. R., Jones, D. O., Kenworthy, W. D., et al. 2022, *ApJ*, 939, 11, doi: [10.3847/1538-4357/ac93f9](https://doi.org/10.3847/1538-4357/ac93f9)
- Polletta, M., Nonino, M., Frye, B., et al. 2023, *A&A*, 675, L4, doi: [10.1051/0004-6361/202346964](https://doi.org/10.1051/0004-6361/202346964)
- Refsdal, S. 1964, *MNRAS*, 128, 307
- Rodney, S. A., Brammer, G. B., Pierel, J. D. R., et al. 2021, *Nature Astronomy*, 5, 1118, doi: [10.1038/s41550-021-01450-9](https://doi.org/10.1038/s41550-021-01450-9)
- Scolnic, D. M., Jones, D. O., Rest, A., et al. 2018, *The Astrophysical Journal*, 859, 101, doi: [10.3847/1538-4357/aab9bb](https://doi.org/10.3847/1538-4357/aab9bb)
- Smith, G. P., Ebeling, H., Limousin, M., et al. 2009, *ApJL*, 707, L163, doi: [10.1088/0004-637X/707/2/L163](https://doi.org/10.1088/0004-637X/707/2/L163)
- Stroe, A., & Savu, V.-N. 2021, *AJ*, 161, 158, doi: [10.3847/1538-3881/abe12a](https://doi.org/10.3847/1538-3881/abe12a)
- Suyu, S. H., Bonvin, V., Courbin, F., et al. 2017, *MNRAS*, 468, 2590, doi: [10.1093/mnras/stx483](https://doi.org/10.1093/mnras/stx483)
- Suyu, S. H., Huber, S., Cañameras, R., et al. 2020, arXiv:2002.08378 [astro-ph], <http://arxiv.org/abs/2002.08378>
- Tripp, R. 1998, *Astronomy and Astrophysics*, 331, 815
- Vega-Ferrero, J., Diego, J. M., Miranda, V., & Bernstein, G. M. 2018, *ApJL*, 853, L31, doi: [10.3847/2041-8213/aaa95f](https://doi.org/10.3847/2041-8213/aaa95f)
- Wang, X., Wang, L., Filippenko, A. V., Zhang, T., & Zhao, X. 2013, *Science*, 340, 170, doi: [10.1126/science.1231502](https://doi.org/10.1126/science.1231502)
- Whiting, E. 1968, *Journal of Quantitative Spectroscopy and Radiative Transfer*, 8, 1379, doi: [10.1016/0022-4073\(68\)90081-2](https://doi.org/10.1016/0022-4073(68)90081-2)
- Windhorst, R. A., Cohen, S. H., Jansen, R. A., et al. 2023, *AJ*, 165, 13, doi: [10.3847/1538-3881/aca163](https://doi.org/10.3847/1538-3881/aca163)
- Zhao, X., Maeda, K., Wang, X., & Sai, H. 2021, *MNRAS*, 503, 4667, doi: [10.1093/mnras/staa3985](https://doi.org/10.1093/mnras/staa3985)

## APPENDIX

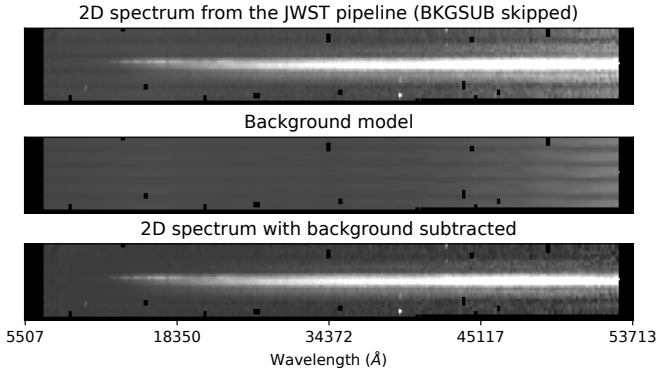


**Figure A1.** An example of the background subtraction. The top panel shows the 2D spectrum from the *JWST* pipeline with the background-subtraction step (BKGSUB) skipped. The middle panel shows the background model from the local-minimum-flux method. The bottom panel shows the residuals after subtracting the background model from the original spectrum.

#### A. BACKGROUND SUBTRACTION, 2D-SPECTRUM MODELING, AND SOURCE EXTRACTION

Because the MSA slitlets used to observe SN H0pe are occupied by extended sources such as the SN’s host galaxy, the default *JWST* pixel-to-pixel background subtraction based on in-scene and off-scene nods was skipped. In addition, the lack of “blank sky” shutters in this NIRSpec observation makes it hard to obtain a well-defined master background to feed to the *JWST* pipeline for subtraction. Instead, we developed a custom code to evaluate a 2D master background using the local minimum flux in 2D spectra for a given wavelength. In detail, for each pixel in a 2D spectrum without a background subtraction, we calculated the minimum flux from the pixels with MSA shutters in the same position along the slit direction. Because the minimum flux could be biased by bad pixels (e.g., cosmic-ray masks), we smoothed the resulting 2D minimum-flux array along the dispersion direction using a median filter with a width of 10 pixels to give a 2D background model. Figure A1 shows an example of the background subtraction.

Source extraction was based on the optimal extraction algorithm from (Horne 1986) and applied to the background-subtracted 2D spectra. For each wavelength in a 2D spectrum, we evaluated the spatial flux distribution by integrating the 2D spectrum along the slit within a range of nearby wavelengths. We then fit kernel functions (Moffat functions for extended sources and Gaus-

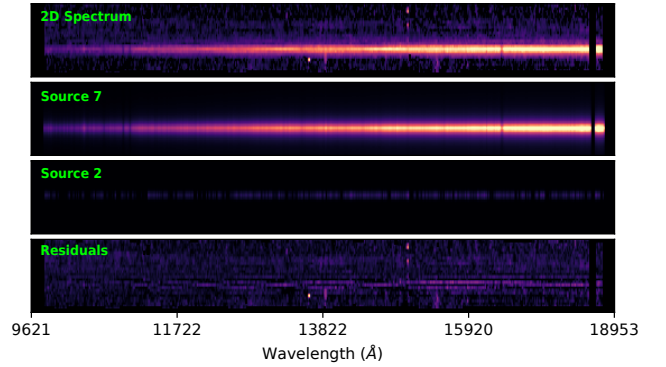


**Figure A2.** G140M spectrum from Slit A. The top panel shows the 2D spectrum from the *JWST* pipeline. The middle two panels show the best-fit models of the host galaxy (Source 7) and the SN (Source 2). The bottom panel shows the residuals after subtracting the galaxy and the SN model from the original spectrum.

sian functions for point-like sources) to the flux distribution of the integrated spectra. For extended sources, we obtained a set of best-fit Moffat functions by scanning over the whole wavelength range. Assuming that the core width of the Moffat functions is linear and the power index of the Moffat functions is a constant over the wavelength direction, we constructed 2D extraction models based on the best-fit core widths and power indexes of Moffat functions. For point-like sources, the extraction Gaussian was fitted to the composite PSFs. For unresolved sources from the NIRSpec observation, we assigned a point-source kernel at the source position. Finally, we fixed the shapes of these kernels at each wavelength and fit the kernels flux simultaneously into the original 2D spectra.

All the 2D spectra taken from Slits A, B, and C are shown in Figures A2 through A9 (except the NIRSpec PRISM spectra from Slit B, which is shown in Figure 2). Labels are source names in the MSA configuration data, where Sources 2, 3, and 4 are SN Images A, B, and C, respectively, and Sources 5, 6, and 7 are images of the SN’s host galaxy for Images B, C, and A, respectively.

#### B. RESULTS OF THE SN-PHASE MEASUREMENTS BEFORE ACCOUNTING FOR SYSTEMATIC ERRORS

Table B1 presents the constraints on the phases of the SN images based on the analyses described in Section 5. These constraints arise either from the deviation of the model parameters within the MCMC chains or from the variation in the templates used by the SNID software

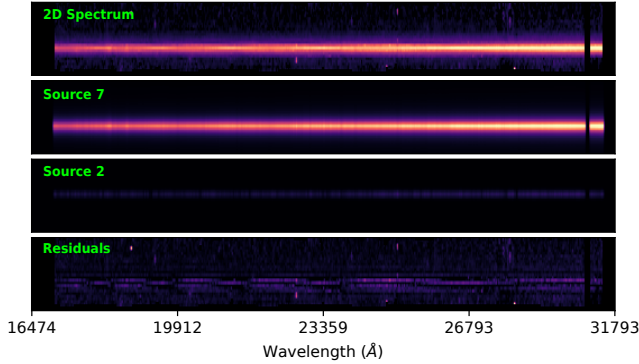


**Figure A3.** G235M spectrum from Slit A. Top panel is the 2D spectrum from the *JWST* pipeline. The middle two panels show the best-fit models of the host galaxy (Source 7) and the SN (Source 2). The bottom panel shows the residuals after subtracting the galaxy and the SN models from the original spectrum.

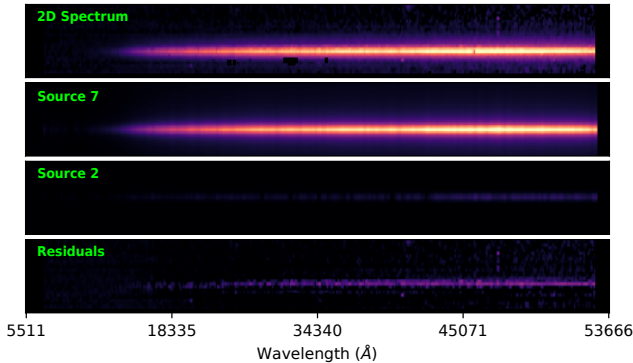


**Figure A4.** PRISM spectrum from Slit A. Top panel shows the 2D spectrum from the *JWST* pipeline. The middle two panels show the best-fit models of the host galaxy (Source 7) and the SN (Source 2). The bottom panel shows the residuals after subtracting the galaxy and the SN models from the original spectrum.

package. The systematic uncertainties derived from our simulations, as described in Section 6, are not included in the error estimates listed in Table B1.

## C. RESULTS FROM THE SALT3-NIR MODEL

### C.1. Joint MCMC fitting

The primary SALT3-NIR fit was simultaneous to all three images of SN H0pe. Shared parameters comprised spectral stretch  $x_1$  and color  $c$ , as described in Section 5.2. Figure C10 shows the posterior distributions of the fitted parameters. The fits constrain  $x_1 = 0.77 \pm 0.23$  and  $c = 0.24 \pm 0.02$ . Figure C11 illustrates the fit uncertainties. Absorption features at rest-frame  $\sim 4000 \text{ \AA}$ ,  $\sim 4900 \text{ \AA}$ , and  $\sim 5600 \text{ \AA}$  in the modeled spectrum at  $t = 50$  days (shown in the bottom panel

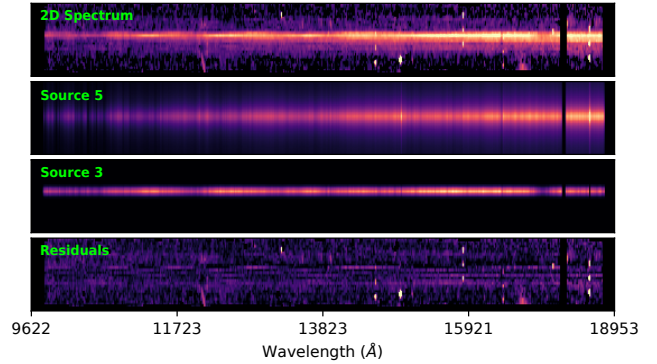


**Figure A5.** G140M spectrum from Slit B. Top panel shows the 2D spectrum from the *JWST* pipeline. The middle two panels show the best-fit models of the host galaxy (Source 5) and the SN (Source 3). The bottom panel shows the residuals after subtracting the galaxy and the SN models from the original spectrum.

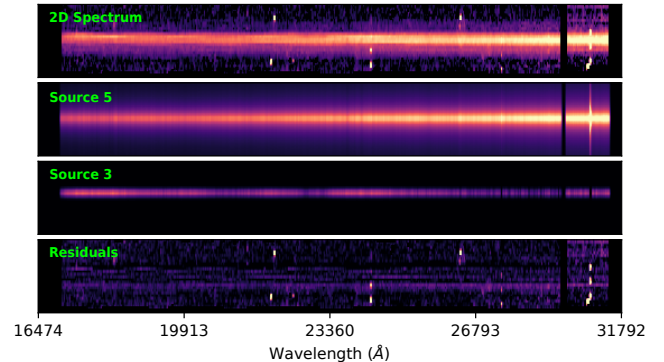


**Figure A6.** G235M spectrum from Slit B. Top panel shows the 2D spectrum from the *JWST* pipeline. The middle two panels show the best-fit models of the host galaxy (Source 5) and the SN (Source 3). The bottom panel shows the residuals after subtracting the galaxy and the SN models from the original spectrum.

of Figure C11) are likely artifacts due to the model approaching its 50-day phase boundary. No such features have been observed in previous SN Ia spectra.

### C.2. Simulation of the model fitting

We tested the SALT3-NIR results using simulations similar to those outlined in Section 6. Figure C12 shows inferred versus actual phases for joint fits to a set of nearby SNe Ia. The uncertainties are about the same as those of the Hsiao07 fits for phases  $\lesssim 30$  days, and systematic offsets in that range are negligible. At later phases, the inferred phases tend to be a little later than the true phases but consistent with equality within the larger uncertainties.

Table B1. SN H0pe Image Phases

	Image A	Image B	Image C
Hsiao (joint)	$52.5^{+11.0}_{-11.4}$	$5.6^{+0.4}_{-0.4}$	$26.0^{+1.0}_{-0.8}$
Hsiao (independent)	$43.4^{+22.2}_{-22.4}$	$5.9^{+0.5}_{-0.6}$	$26.9^{+1.1}_{-1.0}$
SALT3-NIR (joint)	$45.1^{+6.1}_{-8.2}$	$4.2^{+1.1}_{-1.0}$	$27.5^{+0.8}_{-0.7}$
SALT3-NIR (independent)	$36.9^{+7.7}_{-9.0}$	$4.9^{+0.7}_{-1.1}$	$27.8^{+2.2}_{-0.8}$
SNID (templates 2.0)	...	$0.5^{+4.2}_{-4.2}$	$25.8^{+13.7}_{-13.7}$
SNID (Ia-norm templates)	...	$0.3^{+4.3}_{-4.3}$	$23.3^{+13.3}_{-13.3}$
SNID (SALT3-NIR spectra)	...	$5.0^{+6.8}_{-6.8}$	$26.0^{+12.6}_{-12.6}$

NOTE—Phases are rest-frame days after the peak brightness, and uncertainties are  $1\sigma$ . For fits to the Hsiao07 templates and the SALT3-NIR model, the listed uncertainties encompass solely the dispersion within their respective MCMC samples.

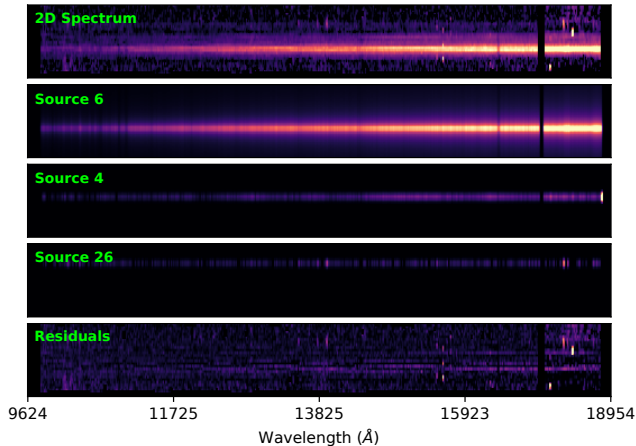


**Figure A7.** G140M spectrum from Slit C. Top panel shows the 2D spectrum from the *JWST* pipeline. The middle three panels show the best-fit models of the host galaxy (Source 6), the SN (Source 4), and a nearby arc (Source 26). The bottom panel shows the residuals after subtracting the galaxy and the SN models from the original spectrum.

### C.3. Constraints on time delays and magnifications

We repeated the Section 7 analysis using the SALT3-NIR model, fixing the spectral stretch and color parameters  $x_1$  and  $c$  to the best-fit values. The resulting constraints on the phases  $t_i$ , time delays  $\Delta t_i$ , and magnifications  $\mu_i$  are shown in Table 6. Values are consistent with those from the Hsiao07 fits within the uncertainties. Calculating absolute magnifications is possible because the luminosities of SNe Ia show small dispersion after correction for light-curve shape and color. For the SALT3-NIR model, we corrected their  $B$ -band magnitudes for the spectral stretch ( $x_1$ ) and color ( $c$ ) based on the Tripp equation (Tripp 1998), and hence the corrected  $B$ -band magnitude ( $\hat{m}_B$ ) is given by  $\hat{m}_B = \mu + M = m_B + \alpha x_1 - \beta c$ , where  $\mu$  is the distance modulus,  $M$  is the absolute  $B$ -band magnitude of a fiducial SN Ia with  $x_1 = 0$  and  $c = 0$ , and  $m_B$  is the measured apparent peak magnitude in rest-frame  $B$ -

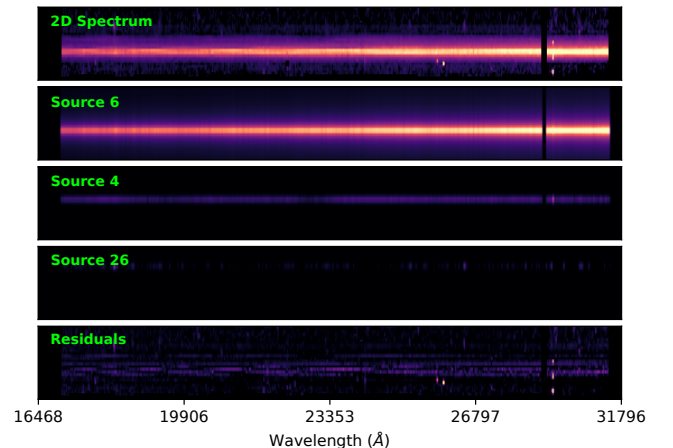


**Figure A8.** G235M spectrum from Slit C. Top panel shows the 2D spectrum from the *JWST* pipeline. The middle three panels show the best-fit models of the host galaxy (Source 6), the SN (Source 4), and a nearby arc (Source 26). The bottom panel shows the residuals after subtracting the galaxy and the SN models from the original spectrum.

band. We used  $\alpha = 0.15$  and  $\beta = 3.0$  from Scolnic et al. (2018) based on the Gaussian intrinsic scatter model of SNe Ia from Guy et al. (2010). Subsequently, comparing  $\hat{m}_B$  from peak SALT3-NIR spectra derived from a set of  $\mathbf{Y}$  parameters from the MCMC chain to the expected  $\hat{m}_B$  based on the complete sample from Scolnic et al. (2018) gave the posterior distributions of the magnifications listed in Table 6. An alternative assumption is that SN H0pe is a standard candle in the rest-frame  $Y$ -band, as described in Section 7. The  $Y$ -band magnitude of a standard SN Ia is characterized by  $x_1 = 0$  and  $c = 0$  and a rest-frame  $B$ -band magnitude equal to the expected  $\hat{m}_B$ . This gave results consistent with the  $B$ -band magnitudes, after applying corrections for spectral stretch and color. The posterior distributions of the SALT3-NIR magnifications are shown in Figure C13, and Table 5 lists the correlation matrices.

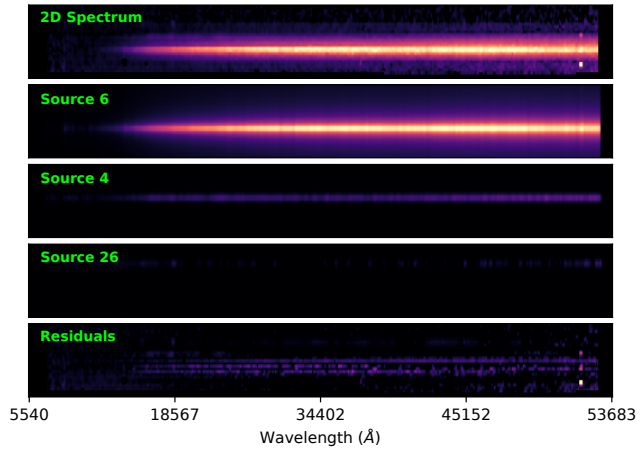


**Figure A9.** PRISM spectrum from Slit C. Top panel shows the 2D spectrum from the *JWST* pipeline. The middle three panels show the best-fit models of the host galaxy (Source 6), the SN (Source 4), and a nearby arc (Source 26). The bottom panel shows the residuals after subtracting the galaxy and the SN model from the original spectrum.



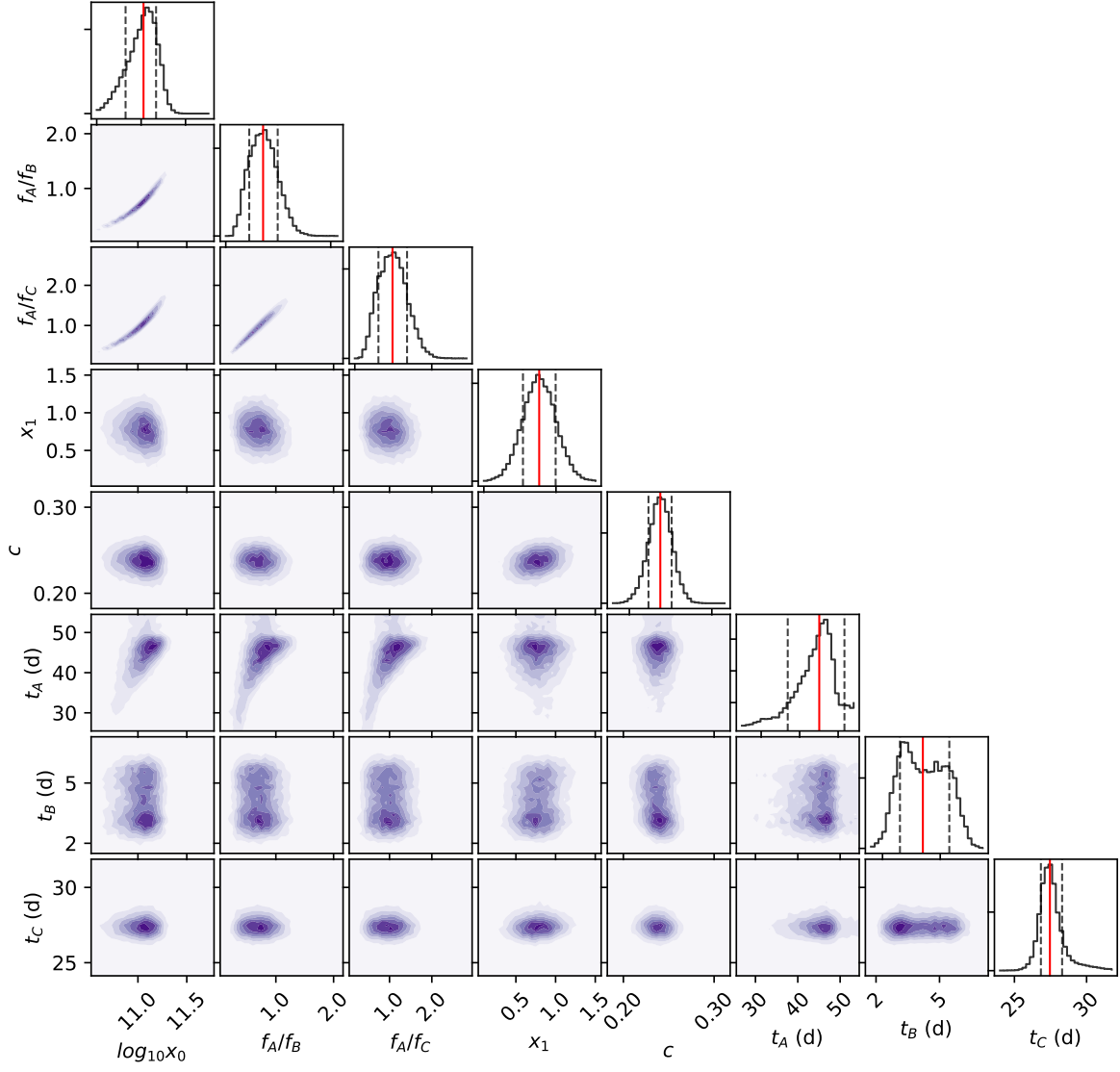


**Figure C10.** Parameter distributions from the SALT3-NIR model fits.  $x_0$ ,  $x_1$  and  $c$  are SALT3-NIR model parameters,  $f_A/f_B$  and  $f_A/f_C$  are the template-flux ratios between Images A and B and between Images A and C, respectively, and  $t_A$ ,  $t_B$ , and  $t_C$  are rest-frame phases of Images A, B, and C, respectively. The solid vertical line on each histogram marks the median of the parameter, while the dashed vertical lines denote the 68% confidence interval of each distribution.

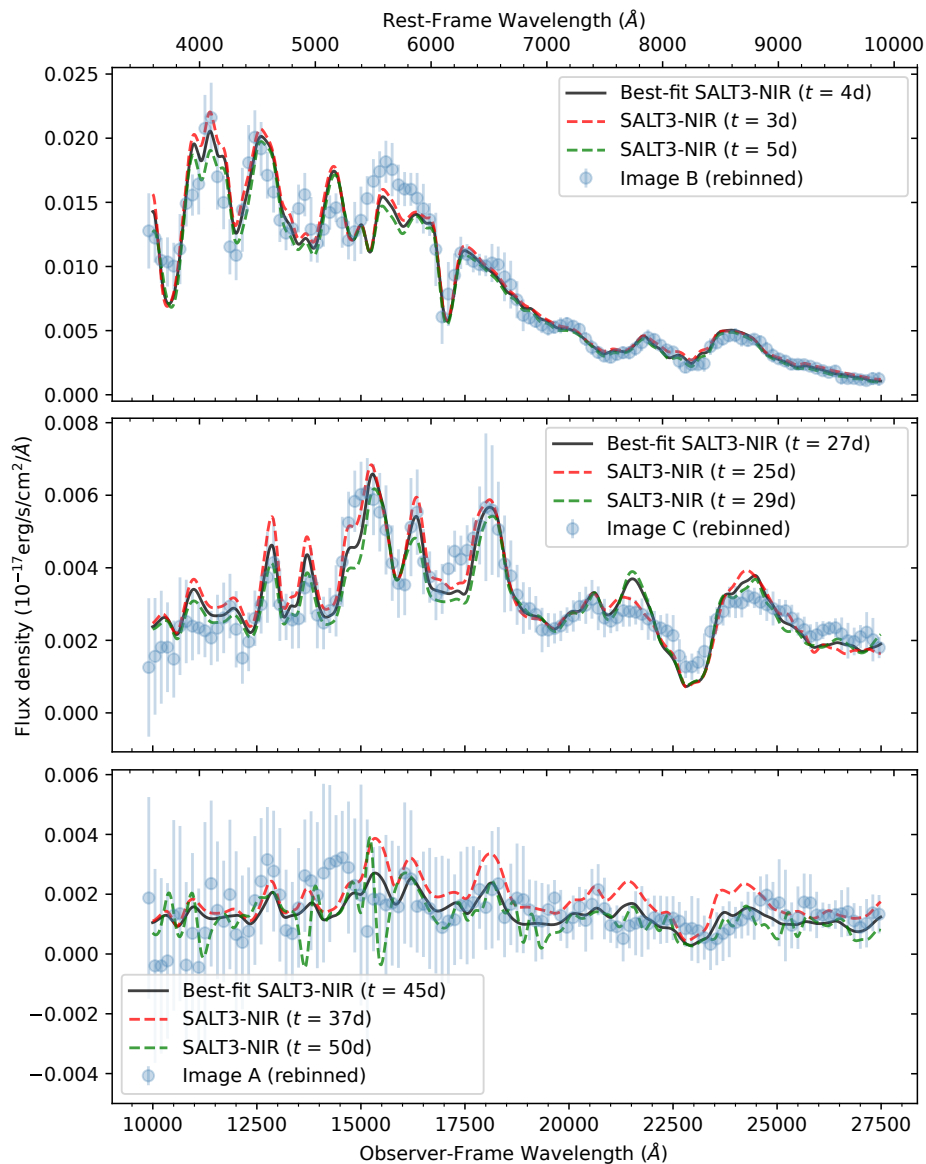


**Figure C11.** Best-fit SALT3-NIR models from Figure 5 are depicted again here, including the models for SN phases that deviate by  $\pm 1\sigma$  (rounded to the nearest integers) from the best-fit phases. Data points and error bars show the observed ( $120\text{\AA}$ -rebinned) SN H0pe spectra.

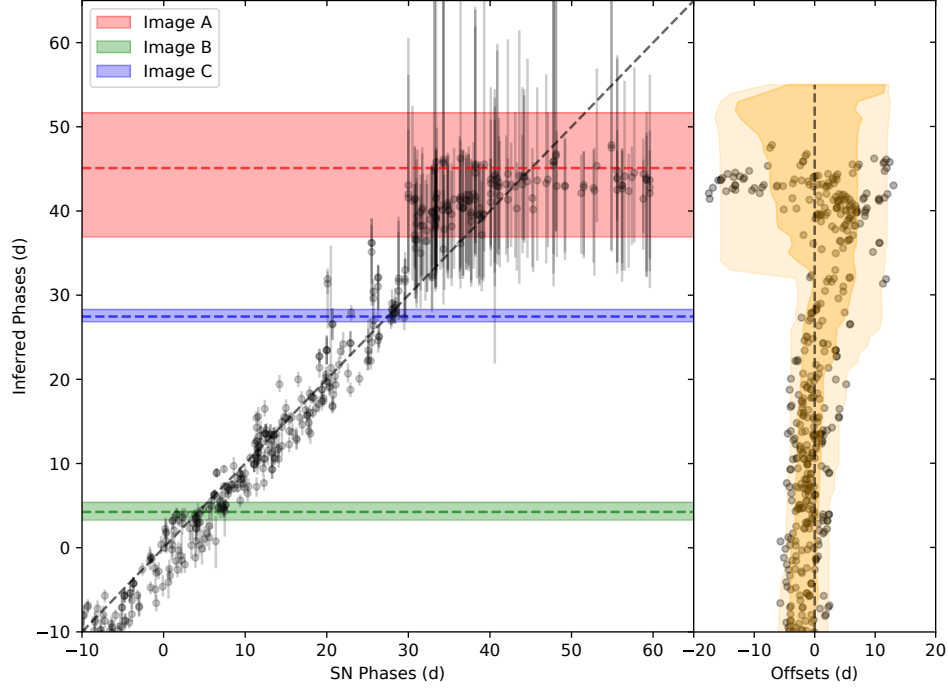


**Figure C12. Left:** inferred phases from SALT3-NIR fitting versus actual phases of a set of nearby SNe Ia. Error bars correspond to the 68% confidence intervals of the inferred phases. Horizontal dashed lines and shaded regions mark the inferred phases and their 68% confidence intervals for the three images of SN H0pe. The diagonal dashed line shows equality. **Right:** deviation of the best-fit inferred phase from the actual phase. Shaded regions mark the 68% (darker) and 95% (lighter) confidence intervals of the residuals measured within a 10-day rolling window.

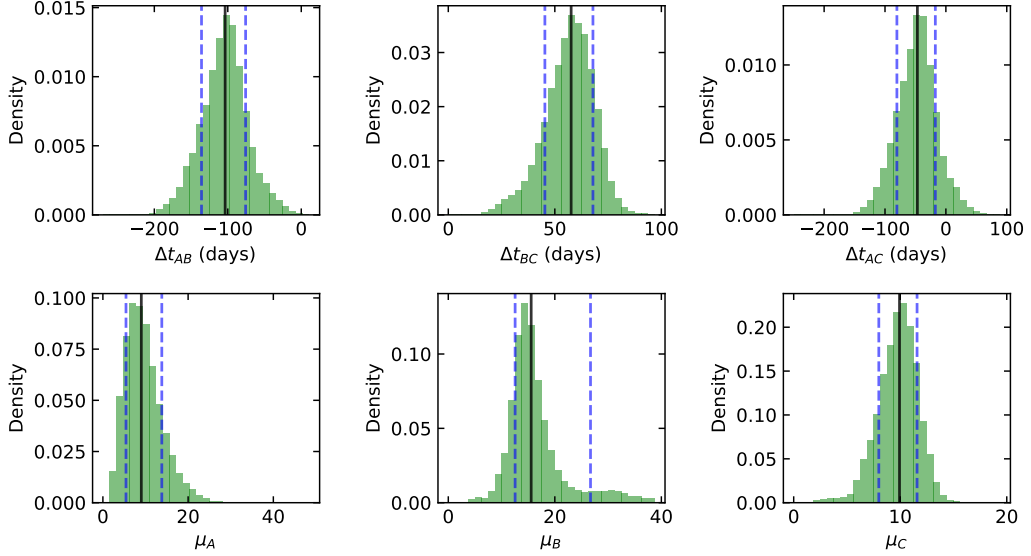


**Figure C13.** Posterior probability densities of the relative time delays and the macro lens' magnifications between SN H0pe's images. Histogram shows values derived from the SALT3-NIR model. The distributions integrate the uncertainty from the MCMC fitting with systematic uncertainties, estimated from the model fitting of nearby SN Ia spectra and from the simulated SN Ia spectra. The uncertainties take into account the impacts of microlensing and millilensing effects.